Table 1
Specific surface areas and average crystallite sizes of the TiO_2 samples obtained from various synthesis conditions

Sample	Amount of TNB in solvent (g)	Temperature (°C)	Holding time (h)	Crystallite size (nm)	Specific surface area (m^2/g)		S_1/S_2
					S_1[a]	S_2[b]	
1	15	300	0.5	9.0	126.4	170.9	0.74
2	25	300	2.0	11.0	92.3	139.9	0.66
3	25	320	6.0	12.5	78.2	123.1	0.64
4	25	350	6.0	14.5	53.1	106.1	0.50
5	25	350	8.0	15.0	51.1	102.6	0.50

[a] S_1 is specific surface area determined from N_2 physisorption results.
[b] S_2 is specific surface area calculated based on the correlation between surface area and crystallite size of TiO_2 ($S_2 = 6/d\rho$ [29]).

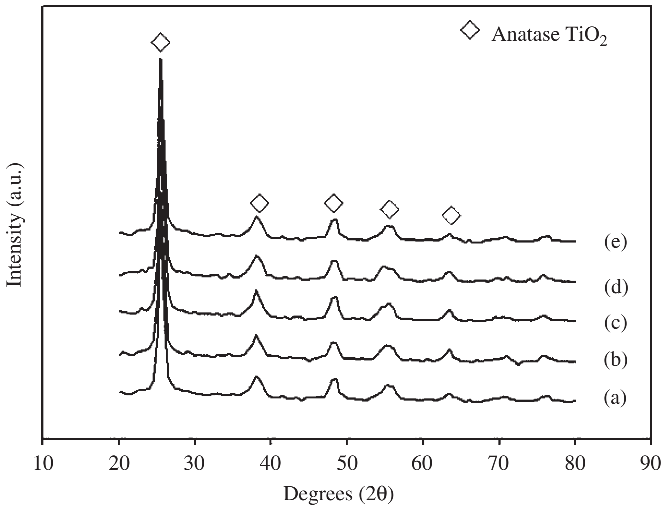

Fig. 1. XRD patterns of the TiO_2 samples with various crystallite sizes (a) 9 nm, (b) 11 nm, (c) 12.5 nm, (d) 14.5 nm, and (e) 15 nm.

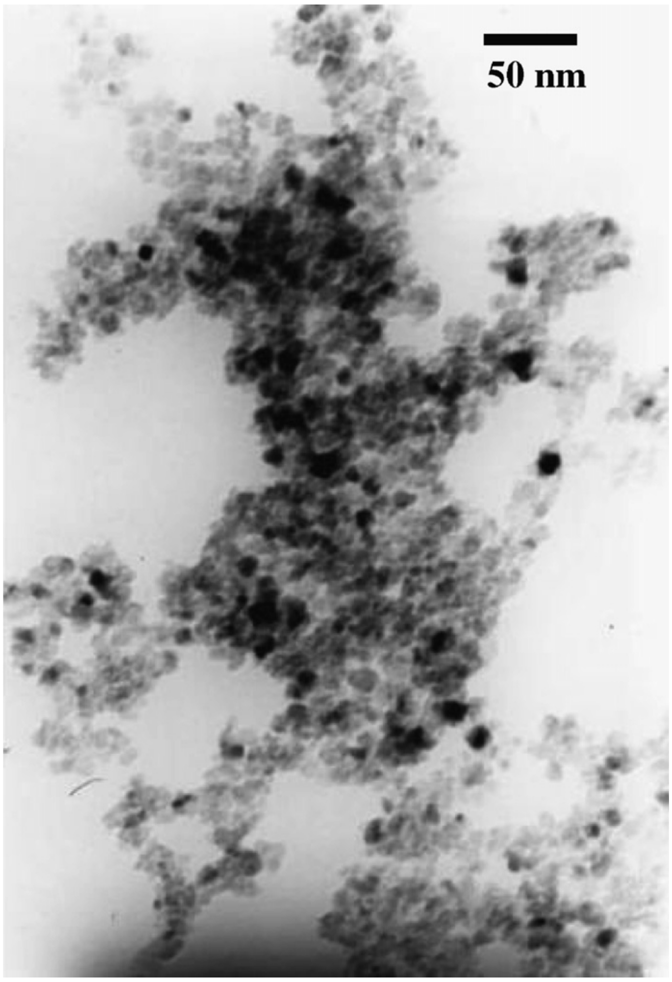

Fig. 2. A typical TEM micrograph of the TiO_2-9 nm sample.

obtained by solvothermal synthesis under the conditions used consist of spherical particles with particle sizes consistent with the calculated results. The TiO_2 samples may contain a fraction of amorphous phase since the preferential orientation of TiO_2 nanoparticles was not clearly seen; however, it is probably due to the moderate magnification used. In order to elucidate the structure of TiO_2 nanocrystallites, a high-resolution transmission electron microscope with selected area electron diffraction (SAED) may be needed.

Temperature-programmed desorption profiles of CO_2 from the titania surface are shown in Fig. 3. The titania samples exhibited two desorption peaks at temperatures ca. 183 K and 213 K, which were attributed to the two structures of TiO_2 [30]. The peak at ca. 183 K is attributed to CO_2 molecules bounding to regular five-coordinate Ti^{4+} site, which was considered as the perfect titania structure. The second peak at ca. 213 K has been considered as desorption of CO_2 molecules bounding to Ti^{3+} defect structure. It is clearly seen from the TPD results that the areas of the CO_2 desorption peak at 213 K apparently increased with increasing crystallite size. It is indicated that the larger crystallite size of TiO_2 obtained from solvothermal synthesis possessed a higher amount of Ti^{3+} surface defects. The ratios of peak areas of Ti^{3+}/Ti^{4+} were also determined by curve fitting and area calculation using a SYSTAT Peakfit program and the results are given in Table 2. It was found that the Ti^{3+} density increased with increasing TiO_2 crystallite size from 9 to 14.5 nm. The value of Ti^{3+}/Ti^{4+} for TiO_2-14.5 nm and TiO_2-15 nm was not significantly different.

An example of the ESR results of the solvothermal-derived TiO_2 powders is shown in Fig. 4. All the titania samples exhibited one major signal at a g value of 1.996,

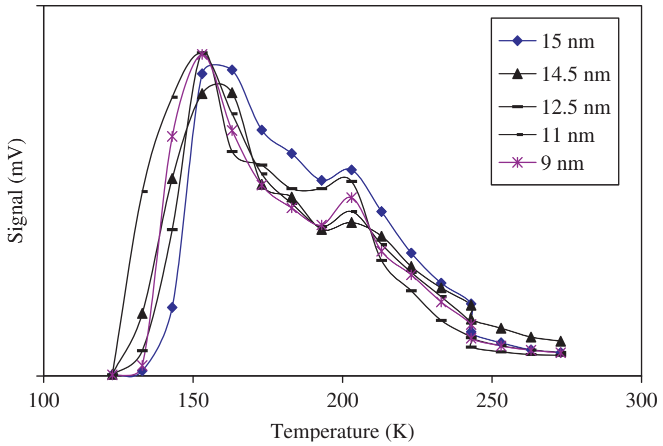

Fig. 3. Thermal desorption spectra for CO_2 adsorbed on the various TiO_2 samples.

Table 2
Ratios of peak areas of Ti^{3+}/Ti^{4+} determined from the CO_2-TPD experiments

Average crystallite size[a] (nm)	Ti^{3+}/Ti^{4+}[b]
9.0	0.923
11.0	1.046
12.5	1.299
14.5	1.580
15.0	1.474

[a] Based on XRD results.
[b] Based on CO_2-TPD results.

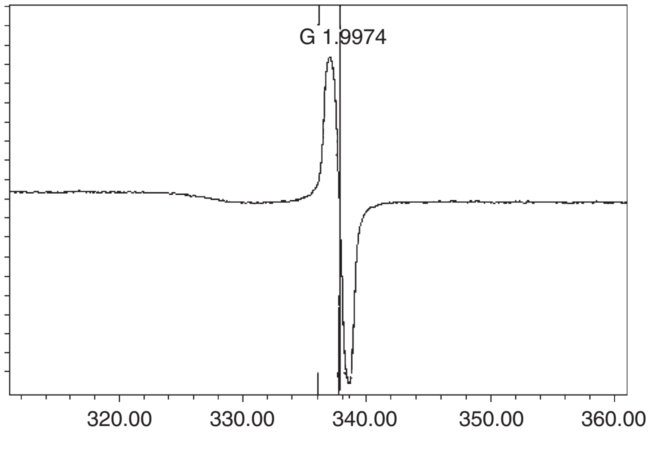

Fig. 4. ESR spectra for various TiO_2 samples.

which can be assigned to Ti^{3+} at titania surface [31–33]. According to Nakaoka and Nosaka [24], there were six ESR signals that occurred on the surface of titania: (i) $Ti^{4+}O^{-}Ti^{4+}OH^{-}$, (ii) surface Ti^{3+}, (iii) adsorbed oxygen (O^{2-}), (iv) $Ti^{4+}O^{2-}Ti^{4+}O^{2-}$, (v) inner Ti^{3+}, and (vi) adsorbed water. Fig. 5 demonstrates a relationship between the intensity of ESR spectra per surface area of the TiO_2 and the TiO_2 average crystallite size. It was found that the amount of surface defect of TiO_2 increased with increasing crystallite size.

Photocatalytic decomposition of ethylene was conducted to assess the photocatalytic activity of TiO_2 samples with various crystallite sizes. The conversion of ethylene as a function of time-on-stream for all the samples is shown in Fig. 6. In this study, 'time-on-stream' is defined as the time that surface of the catalyst was illuminated by UV light using 500 W mercury lamps. Photocatalytic activities of the various TiO_2 crystallite sizes are evidently different; ethylene conversions increased with increasing TiO_2 crystallite sizes. It can be correlated to the different amounts of Ti^{3+} defects on TiO_2 samples, in which the higher the amount of Ti^{3+} present in TiO_2, the higher photocatalytic activity obtained. In photocatalysis, light irradiation of TiO_2 powder with photon energy larger than the band-gap energy produces electrons (e^{-}) and holes (h^{+}) in the conduction band and the valence band, respectively. These electrons and holes are thought to have the respective abilities to reduce and oxidize chemical species adsorbed on the surface of TiO_2 particles. For a photocatalyst to be most efficient, different interfacial electron processes involving e^{-} and h^{+} must compete effectively

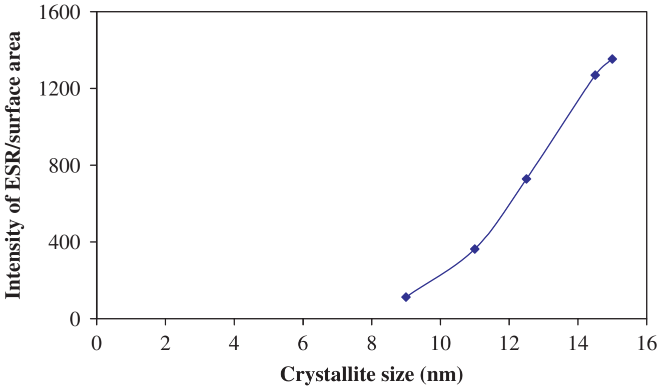

Fig. 5. The intensity of ESR spectra/surface area as a function of TiO_2 crystallite size.

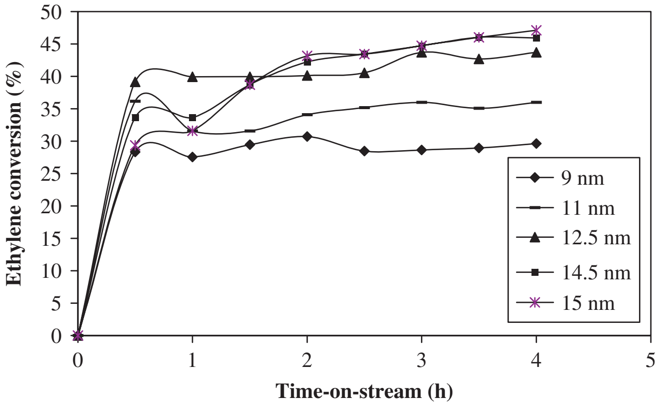

Fig. 6. Photocatalytic activity of the various TiO_2.

with the major deactivation processes involving e^{-}–h^{+} recombination. In general, TiO_2 with higher crystallinity and higher specific surface area typically shows higher photocatalytic activity since the defect of crystal can be the recombination center of the electron–hole pair; hence the photocatalytic activity decreases [1,34,35]. However, the role of Ti^{3+} surface defects on photocatalytic activity of TiO_2 is different from that of crystal (bulk) defect. The Ti^{3+} surface defects serve as traps for photogenerated electrons and consequently prolong lifetime of holes, resulting in higher photocatalytic activity [36–38].

4. Conclusions

This work showed the impact of crystallite size of TiO_2 in the range of 9–15 nm on the Ti^{3+} surface defect present in TiO_2 powders. The amounts of Ti^{3+} defects as determined by ESR and CO_2-TPD were found to increase with increasing crystallite size of TiO_2. The photocatalytic activity of TiO_2 also increased in a similar trend due to an increase in the surface defect/specific surface area of the TiO_2 samples.

Acknowledgments

The authors would like to thank the Thailand Research Fund (TRF), the Commission on Higher Education, and the TJTTP-JBJC for the financial supports of this project.

References

[1] B. Ohtani, Y. Ogawa, S. Nishimoto, J. Phys. Chem. B 101 (1998) 3746.
[2] J.-M. Herrmann, C. Guillard, J. Disdier, C. Lehaut, S. Malato, J. Blanco, Appl. Catal. B-Environ. 35 (2002) 81.
[3] M. Bekbolet, A.S. Suphandag, C.S. Uyguner, J. Photochem. Photobiol. A: Chem. 148 (2002) 121.
[4] J. Aguado, R. Van Grieken, M.J. López-Muñoz, J. Marugán, Catal. Today 75 (2002) 95.
[5] G. Sivalingam, K. Nagaveni, M.S. Hegde, G. Madras, Appl. Catal. B-Environ. 45 (2003) 23.
[6] V.A. Sakkas, I.M. Arabatzis, I.K. Konstantinou, A.D. Dimou, T.A. Albanis, P. Falaras, Appl. Catal. B-Environ. 49 (2004) 195.
[7] D.P. Das, K. Parida, B.R. De, J. Mol. Catal. A-Chem. 240 (2005) 1.
[8] C.-S. Kim, B.K. Moon, J.-H. Park, S.T. Chung, S.-M. Son, J. Crystal Growth 254 (2003) 405.
[9] C. Wang, Z.-X. Deng, G. Zhang, S. Fan, Y. Li, Powder Technol. 125 (2002) 39.
[10] M. Kang, B.-J. Kim, S.M. Cho, C.-H. Chung, B.-W. Kim, G.Y. Han, K.J. Yoon, J. Mol. Catal. A-Chem. 180 (2002) 125.
[11] H. Kominami, M. Kohno, Y. Takada, M. Inoue, T. Inui, Y. Kera, Ind. Eng. Chem. Res. 38 (1999) 3925.
[12] H.-D. Nam, B.-H. Lee, S.-J. Kim, C.-H. Jung, J.-H. Lee, S. Park, Jpn. J. Appl. Phys. 37 (1998) 4603.
[13] C. Su, B.-Y. Hong, C.-M. Tseng, Catal. Today 96 (2004) 119.
[14] P. Yang, C. Lu, N. Hua, Y. Du, Mater. Lett. 57 (2002) 794.
[15] Y. Bessekhouad, D. Robert, J.V. Weber, J. Photochem. Photobiol. A: Chem. 157 (2003) 47.
[16] H. Kominami, J.-I. Kalo, Y. Takada, Y. Doushi, B. Ohtani, S.-I. Nishimoto, M. Inoue, Y. Kera, Catal. Lett. 46 (1997) 235.
[17] O. Carp, C.L. Huisman, A. Reller, Prog. Solid State Chem. 32 (2004) 33.
[18] T. Torimoto, R.J. Fox III, M.A. Fox, J. Electrochem. Soc. 143 (1996) 3712.
[19] V. Shklover, M.-K. Nazeeruddin, S.M. Zakeeruddin, C. Barbé, A. Kay, T. Haibach, W. Steurer, M. Grätzel, Chem. Mater. 9 (1997) 430.
[20] A.-K. Axelsson, L.J. Dunne, J. Photochem. Photobiol. A: Chem. 144 (2001) 205.
[21] G. Liu, J.A. Rodriguez, J. Hrbek, B.T. Long, D.A. Chen, J. Mol. Catal. A-Chem. 202 (2003) 215.
[22] R.F. Howe, M. Gratzel, J. Phys. Chem. 89 (1985) 4495.
[23] R.F. Howe, M. Gratzel, J. Phys. Chem. 91 (1987) 3906.
[24] Y. Nakaoka, Y. Nosaka, J. Photochem. Photobiol. A: Chem. 110 (1997) 299.
[25] U. Diebold, J. Lehman, T. Mahmoud, M. Kuhn, G. Leonardelli, W. Hebenstreit, M. Schmid, P. Varga, Surf. Sci. 411 (1998) 137.
[26] M. Inoue, H. Kominami, T. Inui, J. Chem. Soc. Dalton Trans. (1991) 3331.
[27] T.L. Thompson, O. Diwald, J.T. Yates Jr., J. Phys. Chem. B 107 (2003) 11700.
[28] S.S. Watson, D. Beydoun, J.A. Scott, R. Amal, Chem. Eng. J. 95 (2003) 213.
[29] W. Payakgul, O. Mekasuwandumrong, V. Pavarajarn, P. Praserthdam, Ceram. Inter. 31 (2005) 391.
[30] L.T. Tracy, D. Oliver, T.Y. John, J. Phys. Chem. B 107 (2003) 11700.
[31] K.-R. Park, J. Zhang, K. Ikeue, H. Yamashita, M. Anpo, J. Cataly. 185 (1999) 114.
[32] A. Watterich, A. Hofstaetter, R. Wuerz, A. Scharmann, J. Solid State Commun. 100 (1996) 513.
[33] Y. Zeng, Y. Zheng, S. Yu, K. Chen, S. Zhou, J. Electrochem. Comm. 4 (2002) 293.
[34] K.Y. Jung, S.B. Park, J. Photochem. Photobiol. A: Chem. 127 (1999) 117.
[35] M.I. Litter, Appl. Catal. B-Environ. 23 (1999) 89.
[36] G. Lu, A. Linsebigler, J.T. Yates Jr., J. Phys. Chem. 99 (1995) 7626.
[37] J. Schwitzgebel, J.G. Ekerdt, H. Gerischer, A. Heller, J. Phys. Chem. 95 (1995) 5633.
[38] D. Brinkley, T. Engel, Surf. Sci. 415 (1998) 1001.

Jointly published by
Akadémiai Kiadó, Budapest
and Springer, Dordrecht

React.Kinet.Catal.Lett.
Vol. 88, No. 1, 65–71 (2006)
DOI:10.1556/RKCL.88.2006.1.9

RKCL4741

ROLE OF RUTHENIUM IN THE REDUCTION BEHAVIOR OF RUTHENIUM-PROMOTED COBALT/TITANIA FISCHER-TROPSCH CATALYSTS

Bunjerd Jongsomjit*, Chitlada Sakdamnuson, Joongjai Panpranot and Piyasan Praserthdam

Center of Excellence on Catalysis and Catalytic Reaction Engineering, Department of Chemical Engineering, Faculty of Engineering, Chulalongkorn University, Bangkok 10330 Thailand

Received February 7, 2005; in revised form August 2, 2005; accepted August 5, 2005

Abstract

Role of ruthenium in the reduction behavior of Ru-promoted Co/TiO_2 catalysts was investigated. Ru could facilitate the reduction but had no effect on water production during reduction.

Keywords: Reduction, cobalt catalyst, titania, Fischer-Tropsch

INTRODUCTION

Due to their high activities [1], high selectivity to linear hydrocarbons and low activities for the competitive water-gas shift (WGS) reaction [2,3], supported cobalt (Co) catalyst is considered to be one of the most important catalysts for Fischer-Tropsch synthesis (FTS) as well as carbon monoxide (CO) hydrogenation. During the past decade, titania-supported Co catalysts have been widely investigated by many authors, especially for the application of FTS in a continuously stirred tank reactor (CSTR) [4-6]. In general, to increase the

---

* Corresponding author. E-mail: bunjerd.j@chula.ac.th

0133-1736/2006/US$ 20.00.
© Akadémiai Kiadó, Budapest.
All rights reserved.

catalytic activity of the Co catalysts, many promoters such as ruthenium (Ru), zirconium (Zr), lanthanum (La), rhodium (Rh), boron (B), and platinum (Pt) have been investigated. It has been reported that a variety of these promoters can increase the reducibility of Co, preserve the activity by preventing the formation of coke, exhibit cluster and ligand effects, act as a source of hydrogen spillover and enhance the dispersion. It should be mentioned that the active form of Co catalysts is the reduced Co metal surface atom. Although Ru promotion appears to enhance the rate of FTS, no studies have specifically addressed how Ru promotes the reaction. Understanding how Ru can modify the catalyst properties could lead to the design of more robust and active Co catalysts.

This investigation focused on giving a better understanding of the roles of Ru on reduction behavior of the Ru-promoted Co/TiO_2 catalyst. The impact of Ru promotion on the reducibility of Co in the absence and presence of water vapor was also investigated.

EXPERIMENTAL

Catalyst preparation

The unpromoted-Co/TiO_2 and Ru-promoted (CoRu/TiO_2) catalysts were prepared by the incipient wetness impregnation using cobalt nitrate [$Co(NO_3)\bullet 6H_2O$] and ruthenium(III) nitrosyl nitrate [$Ru(NO)(NO_3)_3$] as precursors. The TiO_2 used contained 81 mol % of anatase phase and 19 mol % of rutile phase (Ishihara Sangyo, Japan). The catalyst samples were dried at 110°C for 12 h and calcined in air at 500°C for 4 h.

Catalyst pretreatments

Standard reduction

Standard reduction of the calcined catalyst was conducted in a fixed-bed flow reactor under differential conditions (no gradient in the catalyst bed) at 1 atm using a temperature ramp from ambient to 350°C at 1°C/min and holding at 350°C for 10 h in a gas flow having a space velocity of 16,000 h^{-1} and consisting of H_2. The high space velocity of the H_2 flow was applied to insure that the partial pressure of water vapor in the catalyst bed produced by cobalt oxide reduction would be essentially zero.

Hydrothermal treatment

In order to evaluate the stability of catalysts and impacts of water vapor during reduction, hydrothermal treatment was also conducted during standard reduction above. In addition, besides using pure H_2, mixtures of H_2 and water vapor (5-10 vol.%) were also applied separately at the same reduction condition as mentioned above.

Catalyst nomenclature

The nomenclature used for the catalyst samples in this study is following:
Co/Ti : Unpromoted cobalt catalyst on the titania support,
CoRu/Ti : Ru-promoted cobalt catalyst on the titania support,
(C) : Calcined catalyst sample,
(RW0), (RW5) and (RW10): Reduced catalyst samples with no water vapor, 5 vol.% of water vapor, and 10 vol.% of water vapor added during standard reduction, respectively.

Catalyst characterization

BET surface area was determined using N_2 adsorption at 77 K in a Micromeritics ASAP 2010.

X-ray diffraction was conducted using a SIEMENS D-5000 X-ray diffractometer with CuK_α ($\lambda = 1.54439$ Å).

The Raman spectra of the samples were collected by projecting a continuous wave laser of argon ion (Ar^+) green (514.532 nm) through the samples exposed to air at room temperature.

Temperature-programmed reduction of calcined samples was carried out using 50 mg of a sample and a temperature ramp from 35 to 800°C at 5°C/min. The carrier gas was 5% H_2 in Ar.

Reaction

CO hydrogenation ($H_2/CO = 10/1$) was performed to determine the overall activity of the catalyst samples. Hydrogenation of CO was carried out at 220°C and 1 atm. A flow rate of $H_2/CO/He = 20/2/8$ cc/min in a fixed-bed flow reactor under differential conditions was used.

Table I

Characteristics and catalytic properties of samples

Samples	BET surface area (m^2/g)[a]	Reducibility (%)[b]	Total H_2 chemisorption (μmol/g cat.)[c]	Reaction rate ($x10^2$ gCH_2 g cat. h^{-1})[d]		CH_4 Selectivity (%)	
				Initial[e]	Steady state[f]	Initial	Steady state
TiO_2	49	-	-	-	-	-	-
Co/Ti-C	34	78	4.8	25	21	94	96
Co/Ti-RW0	32	74	3.3	23	20	94	94
Co/Ti-RW5	32	72	3.2	23	20	98	98
Co/Ti-RW10	30	68	3.0	23	19	95	96
CoRu/Ti-C	37	87	7.5	37	36	99	98
CoRu/Ti-RW0	37	83	6.7	36	36	98	98
CoRu/Ti-RW5	37	77	5.9	36	35	97	97
CoRu/Ti-RW10	36	75	5.2	36	34	99	99

[a] Measurement error ± 5%

[b] Reducibility was measured during TPR at 30-800°C. The reduced samples were recalcined under the original calcination conditions prior to TPR.

[c] H_2 chemisorption was performed to determine the number of reduced Co surface atoms.

[d] CO hydrogenation was carried out at 220°C, 1 atm and $H_2/CO/Ar = 20/2/8$ cm^3/min.

[e] After 5 min of reaction

[f] After 5 h of reaction

RESULTS AND DISCUSSION

The present study was conducted in order to investigate the roles of Ru in the reduction behavior of CoRu/TiO_2 catalysts. The characteristics and catalytic properties during CO hydrogenation are summarized in Table 1. It was observed that upon Co loading and Ru promotion, there was no significant change in the BET surface areas, suggesting no pore blocking or phase changes in the TiO_2 support. The XRD peaks (not shown) of all calcined samples at 26, 37,48, 55, 62, 69, 71 and 75° (TiO_2 in anatase form) and 27, 36, 42 and 57° (TiO_2 in rutile form) were observed. As expected, XRD peaks of Co_3O_4 species were also detected at 36, 46 and 65° after calcination of samples. However, after reduction with or without water vapor added, only diffraction peaks at 37 and 63° corresponding to CoO were observed. Thus, XRD revealed that Ru was well dispersed in the catalyst samples. A similar trend was also observed in Raman spectroscopy as seen for XRD results. It was found that the TiO_2 support exhibited the Raman bands at 640, 514 and 397 cm^{-1} (anatase form) and 445 cm^{-1} (rutile form). The calcined samples showed Raman bands of the TiO_2 support along with two shoulders at 690 and 480 cm^{-1}, assigned to Co_3O_4 species. Raman spectra for all reduced samples exhibited the similar Raman bands as seen for the calcined ones indicating Co_3O_4 on the surface. In order to determine the number of reduced Co metal surface atoms, H_2 chemisorption was performed as seen in Table 1. It indicated that water vapor during reduction apparently resulted in both lesser number of reduced Co metal surface atoms and reducibility due to Co-support compound formation (Co-SCF) as reported in our previous works [7, 8]. It should be noted that Ru promotion may result in enhanced activities during CO hydrogenation without changing selectivity of products due to increased number of reduced Co metal surface atoms. Roles of the Ru promotion can be discussed further based on the TPR profiles as shown in Figs 1 (for the unpromoted catalysts) and 2 (for the Ru-promoted catalysts).

It can be observed that Ru can only facilitate the reduction of cobalt oxide species due to the hydrogen spillover effect resulting in lower reduction temperatures. It is known that water vapor as a byproduct of a reduction process can enhance the Co-SCF [7, 8]. Thus, water vapor was also introduced during reduction in order to investigate the roles of Ru promotion as well. As seen from Figs 1 and 2, increased amounts of water vapor during reduction had no effect on the reduction behavior of both unpromoted catalysts and Ru-promoted catalysts, indicating no shift of reduction temperatures. In summary, Ru promotion can only facilitate the reduction of cobalt oxide species but has no effect on water vapor produced during reduction.

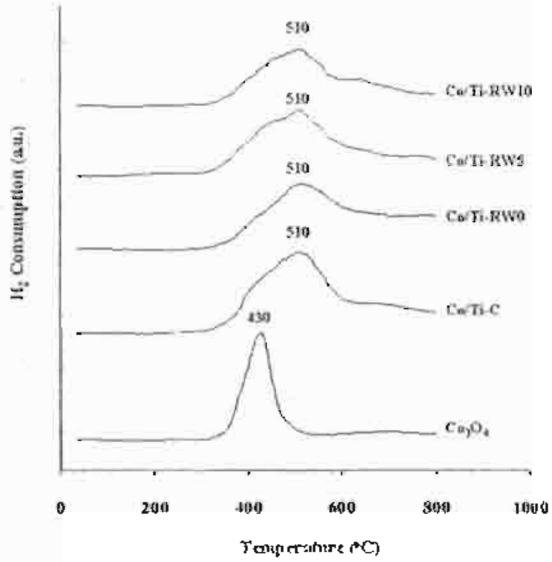

Fig. 1. TPR profiles of the unpromoted cobalt catalysts

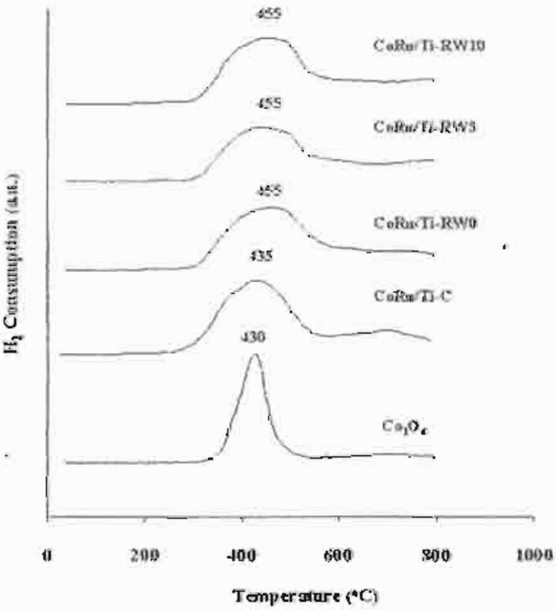

Fig. 2. TPR profiles of the Ru-promoted cobalt catalysts

Acknowledgements. We gratefully acknowledge the financial support by the National Research Council of Thailand (NRCT), the Thailand Research Fund (TRF) and Thailand-Japan Technology Transfer Project (TJTTP-JBIC). We would like to thank Prof. James G. Goodwin, Jr. at Clemson University, USA for his advice.

References

1. H.P. Wither, Jr., K.F. Eliezer, J.W. Mechell: *Ind. Eng. Chem. Res.*, **29**, 1807 (1990).
2. E. Iglesia: *Appl. Catal. A.*, **161**, 59 (1997).
3. R.C. Brady, R.J. Pettie: *J. Am. Chem. Soc.*, **103**, 1287 (1981).
4. J.L. Li, G. Jacobs, T. Das, B.H. Davis: *Appl. Catal. A.*, **233**, 255 (2002).
5. G. Jacobs, T. Das, Y.Q. Zhang, J.L. Li, G. Racoillet, B.H. Davis: *Appl. Catal. A.*, **233**, 263 (2002).
6. J.L. Li, L.G. Xu, R. Keogh, B.H. Davis: *Catal. Lett.*, **70**, 127 (2000).
7. B. Jongsomjit, J. Panpranot, J.G. Goodwin, Jr.: *J. Catal.*, **204**, 98 (2001).
8. B. Jongsomjit, C. Sakdamnuson, J.G. Goodwin, Jr.: *Catal. Lett.*, **94**, 209 (2004).

Studies in Surface Science and Catalysis, volume 159
Hyun-Ku Rhee, In-Sik Nam and Jong Moon Park (Editors)
© 2006 Elsevier B.V. All rights reserved

Elucidation of reduction behaviors for Co/TiO$_2$ catalysts with various rutile/anatase ratios

Bunjerd Jongsomjit*, Tipnapa Wongsalee, and Piyasan Praserthdam

Center of Excellence on Catalysis and Catalytic Reaction Engineering
Department of Chemical Engineering, Chulalongkorn University
Bangkok 10330 Thailand, *corresponding author: bunjerd.j@chula.ac.th

The present study revealed effects of various rutile/anatase ratios in titania on the reduction behaviors of titania-supported cobalt catalysts. It was found that the presence of rutile phase in titania could facilitate the reduction process of the cobalt catalyst. As a matter of fact, the number of reduced cobalt metal surface atoms, which is related to the overall activity during CO hydrogenation increased.

1. INTRODUCTION

Supported cobalt (Co) catalysts are preferred for Fischer-Tropsch synthesis (FTS) based on natural gas [1] due to their high activities for FTS, high selectivity for long chain hydrocarbons and low activities for the competitive water-gas shift (WGS) reaction. Many inorganic supports such as silica, alumina, titania and Zeolites have been extensively studied for supported Co catalysts for years. It is known that in general, the catalytic properties depend on reaction conditions, catalyst compositions, types of inorganic supports and the degrees of metal dispersion as well. It is reported that during the past decades, titania-supported Co catalysts have been investigated widely by many authors, especially for the application of FTS in a continuously stirred tank reactor (CSTR) [2-4]. However, it should be noted that titania itself has different crystalline phases such as anatase, brookite and rutile phase. Thus, the differences in compositions of crystalline phases could result in changes on physical and chemical properties of titania, then consequently for the dispersion of cobalt. In order to give a better understanding of those, the focus of this present study was to investigate the cobalt dispersion on titania consisting various ratios of rutile/anatase. The Co/TiO$_2$ was prepared and then characterized using different characterization techniques.

2. EXPERIMENTAL

2.1 Material preparation

Preparation of titania support

The various ratios of rutile:anatase in titania support were obtained by calcination of pure anatase titania (obtained from Ishihara Sangyo, Japan) in air at temperatures between 800-1000°C for 4 h. The high space velocity of air flow (16,000 h^{-1}) insured the gradual phase transformation to avoid rapid sintering of samples. The ratios of rutile:anatase were determined by XRD according to the method described by Jung et al. [5] as follows:

$$\% \text{Rutile} = \frac{1}{[(A/R)0.884 + 1]} \times 100$$

Where, A and R are the peak area for major anatase ($2\theta = 25^\circ$) and rutile phase ($2\theta = 28^\circ$), respectively.

Preparation of catalyst samples

A 20 wt% of Co/TiO_2 was prepared by the incipient wetness impregnation. A designed amount of cobalt nitrate $[Co(NO_3)\bullet 6H_2O]$ was dissolved in deionized water and then impregnated onto TiO_2 containing various ratios of rutile:anatase obtained from above. The catalyst precursor was dried at 110°C for 12 h and calcined in air at 500°C for 4 h.

2.2 Catalyst nomenclature

The nomenclature used for the catalyst samples in this study is following:

Rn: titania support containing **n%** of rutile phase (R)

Co/Rn: titania support containing **n%** of rutile phase (R)-supported cobalt

2.3 Catalyst characterization

X-ray diffraction: XRD was performed to determine the bulk crystalline phases of catalyst. It was conducted using a SIEMENS D-5000 X-ray diffractometer with CuK_α (λ = 1.54439 Å). The spectra were scanned at a rate of 2.4 degree/min in the range 2θ = 20-80 degrees.

Scanning electron microscopy and energy dispersive X-ray spectroscopy: SEM and EDX were used to determine the catalyst morphologies and elemental distribution throughout the catalyst granules, respectively. The SEM of JEOL mode JSM-5800LV was applied. EDX was performed using Link Isis series 300 program.

Transmission electron microscopy (TEM): The dispersion of cobalt oxide species on the titania supports were determined using a JEOL-TEM 200CX transmission electron spectroscopy operated at 100 kV with 100k magnification.

Hydrogen chemisorption: Static H_2 chemisorption at 100°C on the reduced cobalt catalysts was used to determine the number of reduced surface cobalt metal atoms. This is related to the overall activity of the catalysts during CO hydrogenation. Gas volumetric chemisorption at 100°C was performed using the method described by Reuel and Bartholomew [6]. The experiment was performed in a Micromeritics ASAP 2010 using ASAP 2010C V3.00 software.

Temperature-programmed reduction: TPR was used to determine the reduction behaviors of the catalyst samples. It was carried out using 50 mg of a sample and a temperature ramp from 35 to 800°C at 5°C/min. The carrier gas was 5% H_2 in Ar. A cold trap was placed before the detector to remove water produced during the reaction.

3. RESULTS AND DISCUSSION

In this present study, we basically showed dependence of the number of reduced cobalt metal surface atoms on dispersion of cobalt oxides along with the presence of rutile phase in titania. Both XRD and SEM/EDX results (not shown) revealed good distribution of cobalt oxides over the titania support. However, it can not differentiate all samples containing various ratios of rutile/anatase phase. Thus, in order to determine the dispersion of cobalt oxide species on titania, a more powerful technique such as TEM was applied with all samples. The TEM micrographs for all samples are shown in Figure 1. The dark spots represented cobalt oxides species present after calcination of samples dispersing on titania consisting various ratios of rutile:anatase. It can be observed that cobalt oxide species were highly dispersed on the titania supports for Co/R0, Co/R3, and Co/R19 samples resulting in an appearance of smaller cobalt oxide patches present. However, the degree of dispersion for cobalt oxide species essentially decreased with increasing the rutile phase in titania from 40 to 99% as seen for Co/R40, Co/R96, and Co/R99 samples resulting in the observation of larger cobalt oxide patches. It was suggested that the presence of rutile phase in titania from 0 (pure anatase phase) to 19% exhibited the highly dispersed forms of cobalt oxide species for the calcined samples. It is known that the active form of supported cobalt catalysts is cobalt metal (Co^0). Thus, reduction of cobalt oxide species is essentially performed in order to transform cobalt oxide species obtained after calcination process into the active cobalt metal atoms for catalyzing the reaction. Therefore, the static H_2 chemisorption on the reduced cobalt samples was used to determine the number of reduced Co metal surface atoms. This is usually related to the overall activity of the catalyst during carbon monoxide (CO) hydrogenation [7].

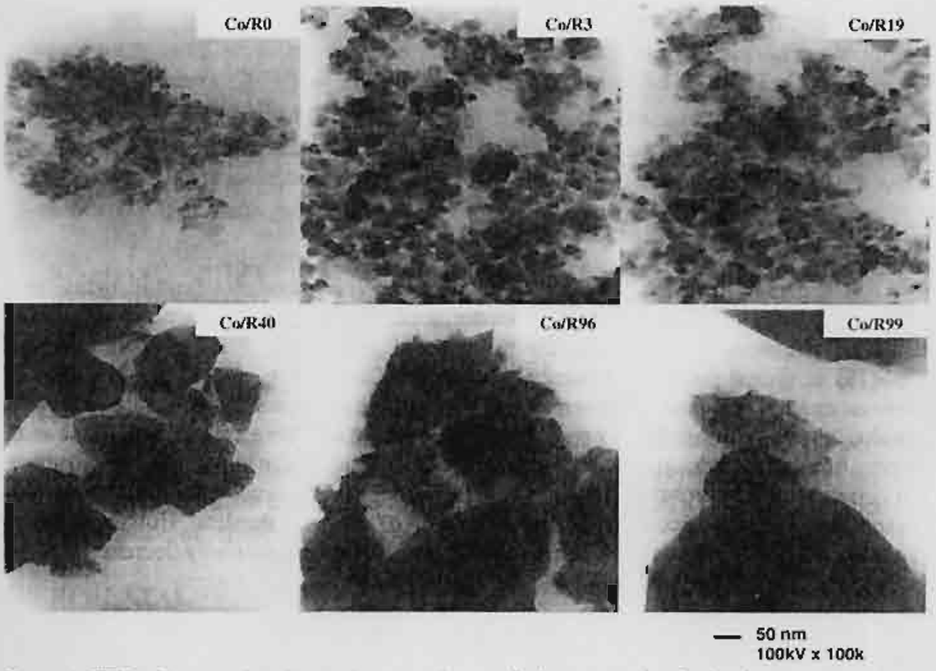

Figure 1 TEM micrographs of samples on various rutile/anatase ratios in titania

The resulted H_2 chemisorption for all samples revealed that the number of the reduced cobalt metal surface atoms increased with the presence of rutile phase in titania up to a maximum at 19% of rutile phase (Co/R19) before decreasing with the greater amounts of rultile phase as shown in **Table 1**. Considering the number of cobalt metal atoms for Co/R0 (pure anatase titania), the number was apparently low even though highly dispersed cobalt oxides species. This was suggested that highly dispersed forms of cobalt oxide species be not only the factor that insures larger number of reduced cobalt metal surface atoms in Co/TiO_2 [8]. On the other hand, it can be observed that the number of reduced cobalt metal surface atoms for Co/R40 and Co/R96 (with the low degree of dispersion of cobalt oxide species as seen by TEM) was larger than that for Co/R0. This was due to the presence of rutile phase in Co/R40 and Co/R96. It should be mentioned that the largest number of reduced cobalt metal surface atoms for the Co/R19 sample was attributed to both highly dispersed cobalt oxide species and the presence of rutile phase in titania. In addition, the resulted TPR as also shown in Table 1 confirmed that the presence of rultie phase could facilitate the reduction of cobalt oxide species by lowering the reduction temperatures. As a result, the number of the reduced cobalt metal surface atoms increased.

Table 1 Resulted H_2 chemisorptiion and reduction temperatures for various Co/TiO_2 samples

Samples	Total H_2 Chemisorption (μmol H_2/g cat.)	Reduction Temperature (°C)
Co/R0	0.93	370
Co/R3	1.55	270
Co/R19	2.44	320
Co/R40	1.66	285
Co/R96	1.71	275
Co/R99	0.69	275

4. SUMMARY

The present research showed a dependence of various ratios of rutile:anatase in titania as a catalyst support for Co/TiO_2 on characteristics, especially the reduction behaviors of this catalyst. The study revealed that the presence of 19% rutile phase in titania for Co/TiO_2 (Co/R19) exhibited the highest number of reduced Co metal surface atoms which is related the number of active sites present. It appeared that the increase in the number of active sites was due to two reasons; i) the presence of rutile phase in titania can facilitrate the reduction process of cobalt oxide species into reduced cobalt metal, and ii) the presence of rutile phase resulted in a larger number of reduced cobalt metal surface atoms. No phase transformation of the supports further occurred during calcination of catalyst samples. However, if the ratios of rutile:anatase were over 19%, the number of active sites dramatically decreased.

ACKNOWLEDGMENT

The financial support from the Thailand Research Fund (TRF) is greatly appreciated.

REFERENCES

[1] H.P. Wither, Jr., K.F. Eliezer, and J.W. Mechell, Ind. Eng. Chem. Res., 29 (1990)1807.
[2] J.L. Li, G. Jacobs, T. Das, and B.H. Davis, Appl. Catal. A., 233 (2002) 255.
[3] G. Jacobs, T. Das, Y.Q. Zhang, J.L. Li, G. Racoillet, and B.H. Davis., Appl. Catal. A., 233 (2002) 263.
[4] J.L. Li,, L.G. Xu, R. Keogh, and B.H. Davis, Catal. Lett., 70 (2000) 127.
[5] K.Y. Jung, and S.B. Park, J. Photochem. Photobio. A: Chem., 127 (1999) 117.
[6] R.C. Reuel, and C.H. Bartholomew, J. Catal., 85(1984) 63.
[7] B. Jongsomjit, C. Sakdamnuson, J.G. Goodwin, Jr., and P. Praserthdam, Catal. Lett., 94 (2004) 209.
[8] B. Jongsomjit, T. Wongsalee, and P. Praserthdam, Mater. Chem. Phys., 92 (2005) 572.

ELSEVIER

Chemical Engineering Science 62 (2007) 899–905

Chemical
Engineering Science

www.elsevier.com/locate/ces

Shorter Communication

Effect of nano-SiO_2 particle size on the formation of LLDPE/SiO_2 nanocomposite synthesized via the in situ polymerization with metallocene catalyst

Ekrachan Chaichana, Bunjerd Jongsomjit*, Piyasan Praserthdam

Center of Excellence on Catalysis and Catalytic Reaction Engineering, Department of Chemical Engineering, Faculty of Engineering, Chulalongkorn University, Bangkok 10330, Thailand

Received 4 July 2006; received in revised form 9 October 2006; accepted 9 October 2006
Available online 17 October 2006

Abstract

Here, we revealed the effect of particle size of the nanoscale SiO_2 on catalytic and characteristic properties of LLDPE/nano-SiO_2 composites synthesized via the in situ polymerization with a zirconocene/MAO catalyst. In the experiment, SiO_2 (10 and 15 nm) was first impregnated with MAO. Then, copolymerization of ethylene/1-hexene was performed in the presence of nano-SiO_2/MAO to produce LLDPE/nano-SiO_2 composites. It was found that the larger particle exhibited higher polymerization activity due to fewer interactions between SiO_2 and MAO. The larger particle also rendered higher insertion of 1-hexene leading to decreased melting temperature (T_m). There was no significant change in the LLDPE molecular structure by means of ^{13}C NMR.

© 2006 Elsevier Ltd. All rights reserved.

Keywords: Nanoscale SiO_2; LLDPE; Polymerization; Metallocene; Polymer composite

1. Introduction

It is known that the copolymerization of ethylene with higher 1-olefins is a commercial importance for production of elastomer and linear low-density polyethylene (LLDPE). LLDPE (density 0.920–0.940) is one of the most widely used polyolefins in many applications, especially, for plastic films. However, in some cases, the use of polyolefins and LLDPE is limited by their drawbacks such as low mechanical strength, low thermal resistance, poor optical properties and so on. Hence, in order to improve the specific properties of these polymers, some additives are used to blend with them.

It has been reported that blending polymer with inorganic materials is considered a powerful method to produce new materials called polymer composites or filled polymers. However, due to the significant development in nanotechnologies in the recent years, nanoscale inorganic materials such as SiO_2, Al_2O_3 and TiO_2 have brought much attention to this research field. Therefore, the polymer composites filled with nanoscale fillers are well recognized as polymer nanocomposites. Essentially, the addition of nanoscale fillers into polymers may lead to overcome the drawbacks and produce new materials, which are robust. Basically, there are three methods used to produce the filled polymer: (i) melt mixing; (ii) solution blending; and (iii) in situ polymerization. Due to the direct synthesis via polymerization along with the presence of nanoscale fillers, the in situ polymerization is perhaps considered the most powerful technique to produce polymer nanocomposites with good distribution and dispersion of the fillers inside polymer matrix. Although LLDPE composites have been studied by many authors (Danjaji et al., 2001, 2002; Huang and Zhang, 2003; Nawang et al., 2001; Verbeek, 2002a,b), those polymer samples were only synthesized by the melt mixing and solution blending. Only few research articles have been reported on the LLDPE nanocomposites synthesized via the in situ polymerization with metallocene catalysts (Jongsomjit et al., 2005a).

In the present study, we developed a new technique to synthesize the LLDPE/nano-SiO_2 via the in situ polymerization with zirconocene/MAO catalyst. The effect of nano-SiO_2

---

* Corresponding author. Tel.: +662 2186869; fax: +662 2186877.
E-mail address: bunjerd.j@chula.ac.th (B. Jongsomjit).

0009-2509/$ - see front matter © 2006 Elsevier Ltd. All rights reserved.
doi:10.1016/j.ces.2006.10.005

particle size on characteristics and catalytic properties was investigated.

2. Experimental section

The preparation of LLDPE/nano-SiO_2 composites via in situ polymerization was performed as follows; all chemicals [nano-SiO_2 (10 and 15 nm) from Aldrich, toluene, *rac*-ethylenebis (indenyl) zirconium dichloride [*rac*-$Et(Ind)_2ZrCl_2$] from Aldrich, methylaluminoxane (MAO) donated by Tosoh Akzo, Japan, trimethylaluminum (TMA), ethylene (National Petrochemical, Thailand) and 1-hexene (Fluka Chemie)] were manipulated under an inert atmosphere using a vacuum glove box and/or Schlenk techniques.

The nano-SiO_2 filler was heated under vacuum at 400 °C for 6 h prior to impregnation with MAO. In order to impregnate MAO onto the nano-SiO_2, the method as follows was described. One gram of the nano-SiO_2 was reacted with the desired amount of MAO at room temperature and stirred for 30 min. The solvent was then removed from the mixture. About 20 ml of toluene was added into the obtained precipitate, stirred the mixture for 5 min, and then removed the solvent. This procedure was done for five times to ensure the removal of impurities. Then, the solid part was dried under vacuum at room temperature to obtain white powder of the nano-SiO_2/ MAO. The amount of $[Al]_{MAO}$ in the nano-SiO_2 particles was determined by the energy dispersive X-ray spectroscopy (EDX) as shown in Fig. 1.

The ethylene/1-hexene copolymerization reaction was carried out in a 100 ml semi-batch stainless steel autoclave reactor equipped with a magnetic stirrer. At first, 0.1, 0.2, and 0.3 g of the nano-SiO_2/MAO ($[Al]_{MAO}/[Zr]_{cat} = 1135$, 2270, and 3405, respectively) and 0.018 mol of 1-hexene along with toluene (to make the total volume of 30 ml) were put into the reactor. The desired amount of $Et(Ind)_2ZrCl_2$ and TMA ($[Al]_{TMA}/[Zr]_{cat} = 2500$) was mixed and stirred for 5-min aging at room temperature, separately, then was injected into the reactor. The reactor was frozen in liquid nitrogen to stop reaction for 15 min and then the reactor was evacuated to remove argon. The reactor was heated up to polymerization temperature (70 °C). To start reaction, 0.018 mol of ethylene was fed into the reactor containing the comonomer and catalyst mixtures. After all ethylene was consumed, the reaction was terminated by addition of acidic methanol (0.1% HCl in methanol) and stirred for 30 min. After filtration, the obtained copolymer (white powder) was washed with methanol and dried at room temperature. In order to give a better understanding for the preparation of the LLDPE/SiO_2nanocomposites.

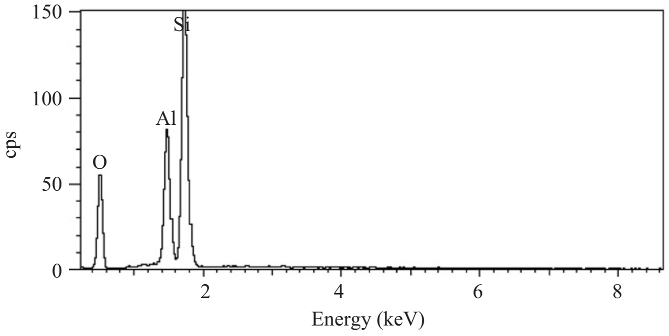

SiO_2	Average wt% of $[Al]_{MAO}$ in SiO_2
10 nm	10.75
15 nm	6.55

Fig. 1. Average amount of $[Al]_{MAO}$ in SiO_2 determined by EDX.

The LLDPE/nano-SiO_2 composites obtained were characterized by means of scanning electron microscopy (SEM) and energy dispersive X-ray spectroscopy (EDX) to identify morphologies and elemental distribution, respectively. Transmission electron microscopy (TEM) was also used to investigate the dispersion of nano-SiO_2 in LLDPE. The molecular structure of LLDPE/nano-SiO_2 composite was obtained using ^{13}C NMR. The melting temperature (T_m) was determined using differential scanning calorimetry (DSC). The molecular weight (MW) and molecular weight distribution (MWD) of the LLDPE fraction were measured using gel permeation chromatography (GPC).

3. Results and discussion

Prier to XRD measurement, the sample was mounted on an adhesive carbon tape as pellets. They were prepared in a glove box and transferred under inert atmosphere. The XRD patterns for the nano-SiO_2 before and after impregnation with MAO (not shown) exhibited the similar XRD patterns indicating only broad XRD band of the amorphous SiO_2. After impregnation of MAO onto the SiO_2, no XRD peaks of $[Al]_{MAO}$ were detected indicating highly dispersed form of it being present. By means of EDX as shown in Fig. 1, it was found that the average amounts of $[Al]_{MAO}$ on 10 and 15 nm-SiO_2 were 10.75 and 6.55 wt%, respectively. Thus, in order to keep the similar ratios of $[Al]_{MAO}/[Zr]_{cat}$ for each nano-SiO_2, the amounts of catalyst used needed to be adjusted. After the in situ polymerization was done, the polymerization time and yield were recorded. They are listed in Table 1 along with some other characteristics of polymers. It can be observed that the total polymer yield for two of the runs was considerably less than 0.5 g. Besides, the ethylene content of all the products, except for one, made with the 15 nm silica particles was < 0.4 g (calculated from the yield and the 1-hexene content of product). The low yields found in two of the runs should be due to two possible factors according to the effect of SiO_2 size: (1) the deactivation of catalyst occurred at a certain time after polymerization, and (2) the chain transfer was prevailed resulting in only oligomers obtained, then they were washed out during filtration. To better illustrate the effect of particle size of nano-SiO_2 on the activities at the same amounts of it, a plot of activity versus the weight of nano-SiO_2 used corresponding to different ratios of $[Al]_{MAO}/[Zr]_{cat}$ is shown in Fig. 2. It can be observed that increased amounts of nano-SiO_2 resulted in increased activities during polymerization for both 10 and 15 nm-SiO_2. This can be attributed to an increase in the $[Al]_{MAO}/[Zr]_{cat}$ ratios from 1135 to 2270 and, then to 3405 corresponding to 0.1, 0.2, and

Table 1
Activity and characteristics of LLDPE-SiO_2 nanocomposites

Filler	Weight (g)	Polymerization Yield (g)	Time (s)	Activity[a]	%SiO_2[b]	T_m[c](°C)	1-Hexene insertion[d] (%)
Nano-SiO_2 (10 nm)	0.1	0.1355	1714	811	37.9	102.3	25.7
	0.2	0.9164	326	28,827	16.0	70.4	47.7
	0.3	0.8633	330	26,827	23.0	86.3	38.7
Nano-SiO_2 (15 nm)	0.1	0.5505	400	23,163	14.4	99.6	29.7
	0.2	0.9555	149	107,930	16.2	89.7	54.5
	0.3	1.002	134	125,853	21.6	87.7	65.0

[a] Activities (kg of polym/mol of Zr h) were measured at polymerization temperature of 70 °C, [ethylene] = 0.018 mol, [1-hexene] = 0.018 mol, $[Al]_{MAO}/[Zr] =$ 1135 to 3405, $[Al]_{TMA}/[Zr] = 2500$, in toluene with total volume = 30 ml and $[Zr]_{cat} = 0.71 \times 10^{-5}$ M (for 15 nm SiO_2) and 1.17×10^{-5} M (for 10 nm SiO_2).
[b] The amount of SiO_2 present in the LLDPE composites based on yield.
[c] Melting temperature (T_m) was obtained from the DSC measurement.
[d] 1-hexene insertion or incorporation was calculated based on ^{13}C NMR.

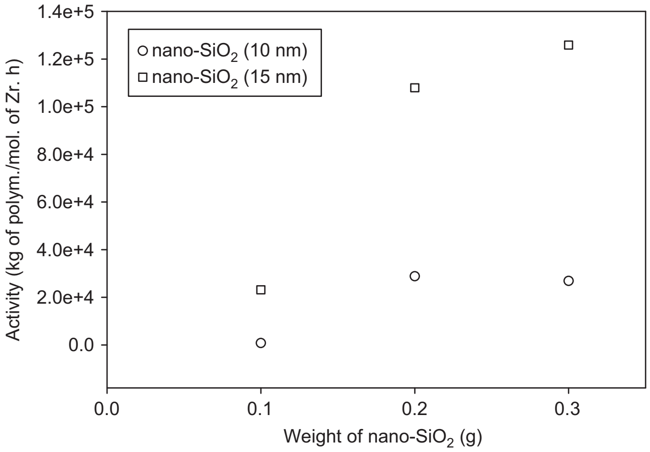

Fig. 2. Activities regarding different particle size and amount added of nano-SiO_2.

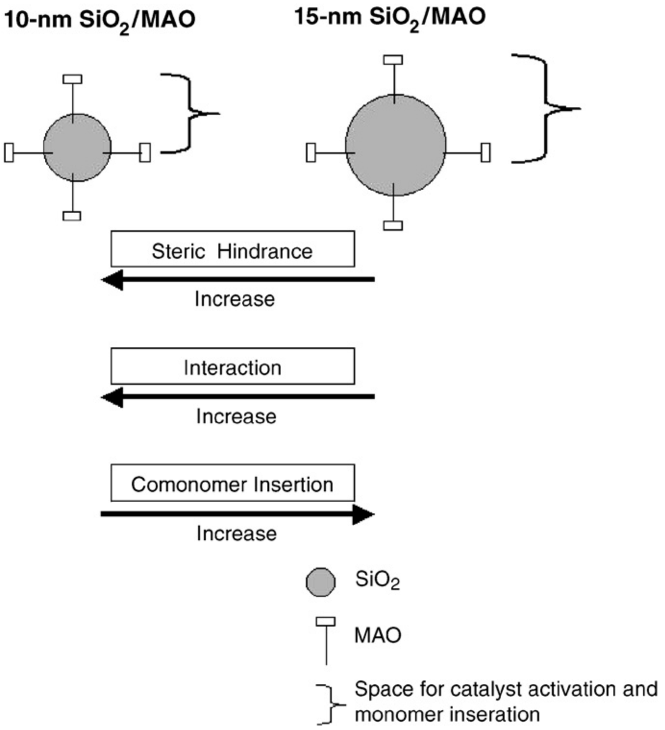

Scheme 1. Conceptual model for impact of nano-SiO_2 particle size on steric hindrance, interaction, and comonomer insertion.

0.3 g of the nano-SiO_2, respectively. It was reported that the greater amounts of MAO resulted in more active species being present during polymerization (Jongsomjit et al., 2004a,b). It was proposed that MAO possibly had many functions, such as an alkylating agent, a stabilizer for a cationic metallocene alkyl and/or counterion, an ionizing and/or reducing agent for the transition element, and a scavenger for the metallocene catalytic system. However, one of the most important roles of MAO is apparently to prevent the formation of $ZrCH_2CH_2Zr$ species, which is formed via a bimolecular process (Chao et al., 2003).

Considering, activities for both 10 and 15 nm-SiO_2, it was found that the 15 nm-SiO_2 exhibited higher activities with the same ratios of $[Al]_{MAO}/[Zr]_{cat}$ as seen in Fig. 2. The higher activities can be attributed to fewer interactions between SiO_2 and MAO arising from the larger particles. It should be noted that SiO_2 is one of the materials having strong interaction with species being present on its surface (Kogelbauer et al., 1995). A wide range of variables including particle size, types of material, and pretreatment condition can affect the particle interaction (Jongsomjit et al., 2001). The smaller particles may interact more with MAO resulting in decreased activities because it is more difficult for metallocene to react with the strongly interacted MAO on SiO_2 surface. Besides, the strong interaction between SiO_2 and MAO, it should be mentioned that the smaller particles also render more steric hindrance. In fact, steric hindrance means more bulky (less space). Considering the small and large particles with the same amounts of MAO on them, the gap between the MAO should be larger on the larger particles due to higher external surface areas. Thus, smaller particles should have more steric hindrance than the larger ones. As the result, the insertion of 1-hexene is more difficult due to the steric hindrance (more bulky). It is known that SiO_2 is one of many supports having a strong interaction with species being present on it. A wide range of variables including particle size, nature of adsorbed species, preparation methods and pretreatment conditions can affect the interaction. The effects of particle size and nature of adsorbed species i.e., MAO can be superimposed on each other. Based on the results, it was suggested that the smaller SiO_2 particles may interact more with MAO resulting in lower activity. In order to give a better understanding, a conceptual model for impact of nano-SiO_2 particle size on the steric hindrance, interaction, and comonomer insertion is illustrated as shown in Scheme 1.

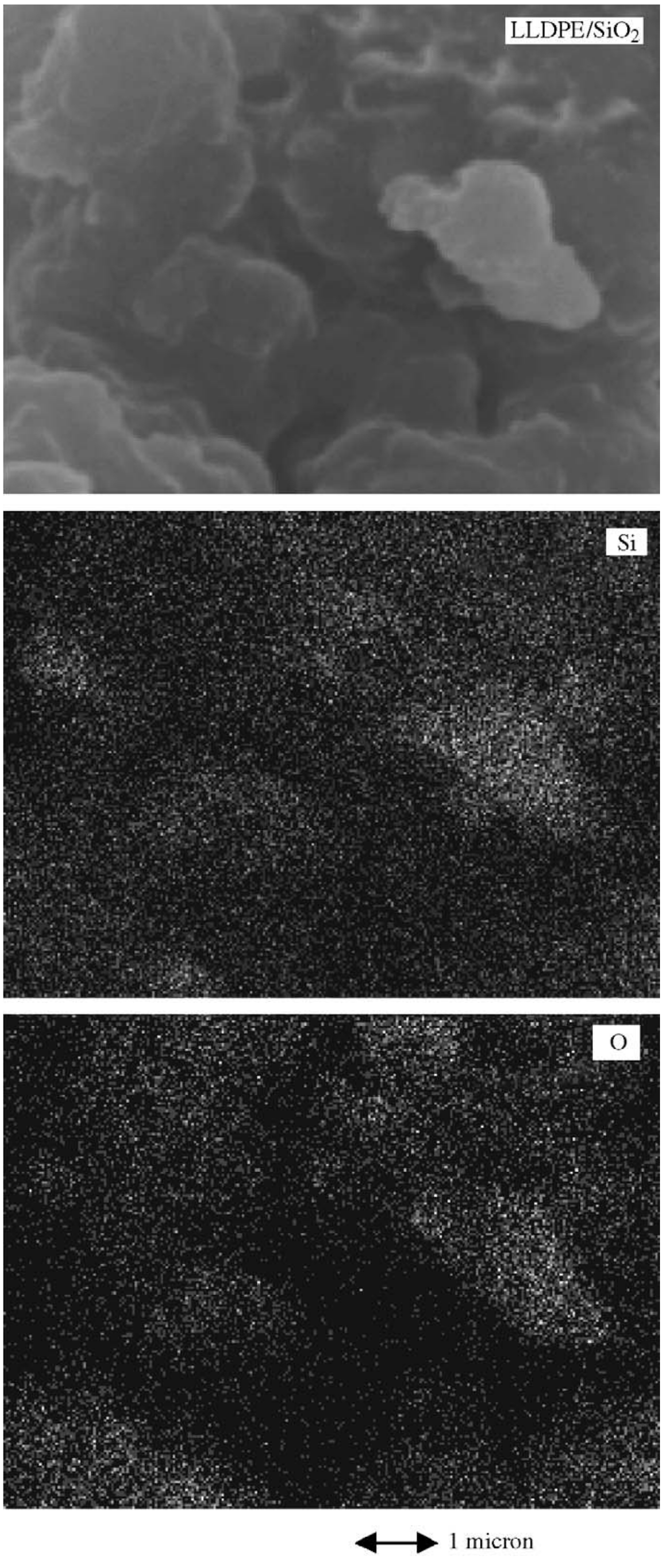

Fig. 3. A typical SEM and EDX images for LLDPE/nano-SiO_2 composites.

The characteristics of LLDPE/nano-SiO_2 were also further investigated. The typical morphologies of LLDPE/nano-SiO_2 composites obtained by SEM and the elemental distribution for Si and O are shown in Fig. 3 . There was no significant change in polymer morphologies for LLDPE nanocomposites containing 10 and 15 nm-SiO_2 with the same amounts of SiO_2. It can be observed that SiO_2 was well distributed in polymer. As known, images from high resolution TEM is an essential component of nanoscience, therefore TEM was performed to identify the dispersion of nano-SiO_2 in LLDPE. The TEM micrographs of LLDPE/nano-SiO_2 are shown in Fig. 4 . Fig. 4a–c represented LLDPE with 10 nm-SiO_2 at 0.1–0.3 g of SiO_2, respectively. Fig. 4d–f showed LLDPE containing 15 nm-SiO_2 at 0.1, 0.2, and 0.3 g of SiO_2, respectively. As seen from both 10 and 15 nm-SiO_2, they appeared as a bunch of spherical-like particles indicating the agglomeration of the primary particles. This was suggested that the poor dispersion being observed. The poor dispersion was due to interaction between particles leading to agglomeration. In addition, there was no pronounced difference among each LLDPE/nano-SiO_2 sample. Thus, in order to obtain well dispersion, the modification of the nano-SiO_2 needs to be further investigated for future work. It has been known that ^{13}C NMR is one of the most powerful techniques to identify the polymer microstructure, especially polyolefins. The resulted ^{13}C NMR spectra (not shown) for all samples were assigned typically to the LLDPE obtained from copolymerization of ethylene/1-hexene. The triad distribution was identified based on the method described by Randall (1989). It can be observed that the LLDPE consisting of 10 and 15 nm-SiO_2 exhibited similar ^{13}C NMR patterns indicating similar molecular structure of polymer. Based on calculations described by Galland et al. (1996), the triad distribution of monomer is listed in Table 2. It indicated that all LLDPE samples were random copolymer with the difference in 1-hexene insertion. This result was also similar with what we found in our previous works without the addition of nano-SiO_2 (Jongsomjit et al., 2004a–c, 2005a–d). According to the triad distribution shown in Table 2, the insertion of 1-hexene can be calculated based on the reference (Galland et al., 1996). The 1-hexene insertion in LLDPE/nano-SiO_2 is shown in Table 1. It can be observed that larger particle resulted in increased 1-hexene insertion due to less steric hindrance. Hence, with larger particles, the large molecule of 1-hexene can insert more. The melting temperature (T_m) as also shown in Table 1 trended to decrease with more insertion of 1-hexene due to decreased crystallinity. However, it can be observed that the T_m of the nanocomposites of 15 nm-SiO_2 (weight 0.2 and 0.3 g) with higher 1-hexene insertion were higher than those of 10 nm-SiO_2 (weight 0.2 and 0.3 g) with lower 1-hexene insertion as shown in Table 1. This should be addressed that besides the effect of 1-hexene insertion on the T_m, the SiO_2 particles added also affect the T_m of polymer as well. Apparently, while higher 1-hexene insertion resulted in

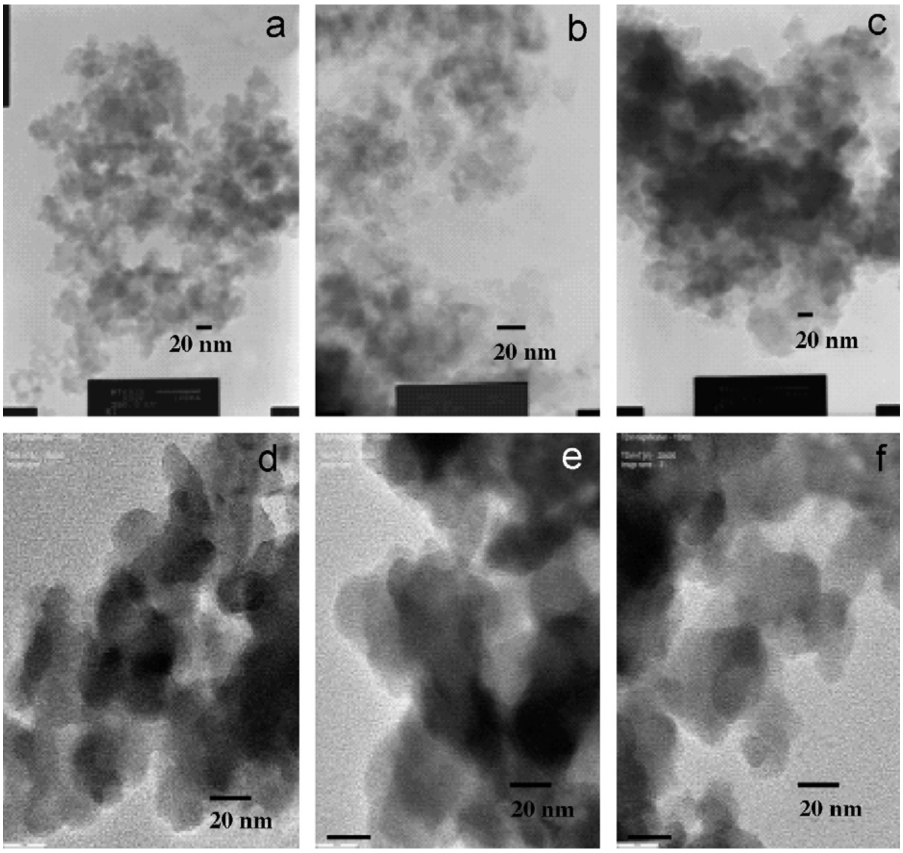

Fig. 4. TEM micrographs of: (a) SiO_2-10 nm, 0.1 g; (b) SiO_2-10 nm, 0.2 g; (c) SiO_2-10 nm, 0.3 g; (d) SiO_2-15 nm, 0.1 g; (e) SiO_2-15 nm, 0.2 g and (f) SiO_2-15 nm, 0.3 g.

Table 2
Triad distribution[a] obtained from ^{13}C NMR of LLDPE-SiO_2 nanocomposites

Filler	Weight (g)	EEE	EEH + HEE	HEH	EHE	EHH + HHE	HHH
Nano-SiO_2 (10 nm)	0.1	0.66	0.09	0	0.04	0.21	0
	0.2	0.39	0.12	0.02	0.06	0.41	0
	0.3	0.47	0.13	0.02	0.07	0.31	0
Nano-SiO_2 (15 nm)	0.1	0.61	0.09	0	0.05	0.25	0
	0.2	0.31	0.12	0.03	0.07	0.47	0
	0.3	0.19	0.12	0.04	0.08	0.57	0

[a] E refers to ethylene and H refers to 1-hexene.

lower T_m, higher content of SiO_2 in polymer rendered higher T_m. It was reported that the particles in polymer matrix can act as nucleating agents (Luyt et al., 2006). Consequently, they increase the crystallinity of polymer. When the particles are too small (i.e., 10 nm-SiO_2), they may locate themselves in the interlamellar spaces, which leave little room for additional crystallization. So, the presence of these particles may even inhibit crystallization. In the case, higher T_m for LLDPE nanocomposites of 15 nm-SiO_2 having higher 1-hexene insertion compared to those of the 10 nm-SiO_2 was essentially observed.

The additional study was conducted by keeping the $[Al]_{MAO}/[Zr]$ ratio (at 2270) constant with changing the catalyst concentrations, [Zr]. Thus, the amounts of nano-SiO_2 can be varied without changing the $[Al]_{MAO}/[Zr]$ ratio. In fact, only 15 nm-SiO_2 was chosen to study the effect of amounts of nano-SiO_2 added. Using the similar ways as mentioned above, the activities and characteristics of LLDPE/15 nm-SiO_2 composite were obtained as shown in Table 3. It was found that at the specified condition the activity went to a maximum with the certain amount of nano-SiO_2 (0.2 g), then went down with increased amount of nano-SiO_2 (0.3 g). Increased activity with increasing the amount of nano-SiO_2 at the beginning can be attributed to increased distribution of MAO. Consequently, this also resulted in increased 1-hexene insertion as seen in Table 3. However, increased more amounts of nano-SiO_2 apparently resulted in decreased activity. This was probably due

Table 3
Activity and characteristics of LLDPE-SiO_2 nanocomposites at $[Al]_{MAO}/[Zr] = 2270$

Filler	Weight (g)	Polymerization Yield (g)	Time (s)	Activity[a]	%SiO_2[b]	T_m [c](°C)	1-Hexene insertion[d] (%)
Nano-SiO_2 (15 nm)	0.1	0.1000	717	4695	46.7	107.6	19.86
	0.2	0.9555	149	107,930	16.2	89.7	54.5
	0.3	0.7545	248	34,136	26.6	101.2	67.5

[a] Activities (kg of polym/mol of Zr h) were measured at polymerization temperature of 70 °C, [ethylene] = 0.018 mol, [1-hexene] = 0.018 mol, $[Al]_{MAO}/[Zr] = 2270$, $[Al]_{TMA}/[Zr] = 2500$, in toluene with total volume = 30 ml and $[Zr]_{cat} = 0.36$ to 1.07×10^{-5} M.

[b] The amount of SiO_2 present in the LLDPE composites based on yield.

[c] Melting temperature (T_m) was obtained from the DSC measurement.

[d] 1-hexene insertion or incorporation was calculated based on ^{13}C NMR.

Table 4
Triad distribution[a] obtained from ^{13}C NMR of LLDPE-SiO_2 nanocomposites

Filler	Weight (g)	EEE	EEH + HEE	HEH	EHE	EHH + HHE	HHH
Nano-SiO_2 (15 nm)	0.1	0.61	0.09	0	0.05	0.25	0
	0.2	0.31	0.12	0.03	0.07	0.47	0
	0.3	0.19	0.12	0.04	0.08	0.57	0

[a] E refers to ethylene and H refers to 1-hexene.

Table 5
MW and MWD of LLDPE fraction in the composites

Filler	Weight (g)	MW ($gmol^{-1}$)	M_n ($gmol^{-1}$)	MWD[a]
Nano-SiO_2 (10 nm)	0.1	38,200	6900	5.5
	0.3	27,200	3400	8.0
Nano-SiO_2 (15 nm)	0.1	41,900	4800	8.7
	0.3	31,700	4000	7.9

[a] MWD was calculated from MW/M_n.

to stronger interaction between the particles. In addition, T_m (Table 3), triad distribution (Table 4) are also present. The effect of nano-SiO_2 particle size on MW and MWD was also investigated as shown in Table 5. In fact, no significant change was observed regarding to the particle size of the nano-SiO_2. Only slight increase in MW with the larger particles was evident. It can be observed that increased amounts of SiO_2 resulted in decreased MW. In addition, a slightly broad MWD was seen for all samples.

4. Summary

Based on this study, it was found that the larger particle (15 nm-SiO_2) exhibited higher activity due to fewer interactions between SiO_2 and MAO. The larger particle also rendered higher insertion of 1-hexene. In particular, higher 1-hexene insertion resulted in decreased melting temperature due to decreased crystallinity. No change in molecular structure of LLDPE was observed. However, the agglomeration of SiO_2 in polymer was seen by TEM. In order to overcome the poor dispersion of particles, the nano-SiO_2 needs to be modified prior to use. Thus, the modification of SiO_2 should be further investigated in the near future.

Acknolwedgments

The authors thank the Thailand Research Fund (TRF), Thailand-Japan Technology Transfer Project (TJTTP-OECF), and the National Science and Technology Development Agency (NSTDA) for the financial support of this project.

References

Chao, C., Praserthdam, P., Khorbunsongserm, S., Rempel, G.L., 2003. Effect of TMA and MAO on ethyelene-propene copolymer using supported zirconocene catalysts. Journal of Macromolecular Science Part A: Pure and Applied Chemistry 40, 181.

Danjaji, I.D., Nawang, R., Ishiaku, U.S., Ismail, H., Mohd Ishak, Z.A., 2001. Sago starch-filled linear low-density polyethylene (LLDPE) films: their mechanical properties and water absorption. Journal of Applied Polymer Science 79, 29.

Danjaji, I.D., Nawang, R., Ishiaku, U.S., Ismail, H., Mohd Ishak, Z.A., 2002. Degradation studies and moisture uptake of sago-starch filled linear low-density polyethylene composites. Polymer Testing 21, 75.

Galland, G.B., Quijada, P., Mauler, R.S., de Menezes, S.C., 1996. Determination of reactivity ratios for ethylene/1-olefin copolymerization catalyzed by the $C_2H_4[Ind]_2ZrCl_2$/methylaluminoxane system. Macromolecular Rapid Communications 17, 607.

Huang, Y.Q., Zhang, Y.Q., 2003. Studies on dynamic mechanical and rheological properties of LLDPE/nano-SiO_2 composites. Journal of Material Science Letters 22, 997.

Jongsomjit, B., Panpranot, J., Goodwin Jr., J.G., 2001. Co-support compound formation in alumina-supported cobalt catalysts. Journal of Catalysis 204, 98.

Jongsomjit, B., Praserthdam, P., Kaewkrajang, P., 2004a. A comparative study of supporting effect during copolymerization of ethylene/1-olefins with silica-supported zirconocene/MAO catalyst. Materials Chemistry and Physics 86, 243.

Jongsomjit, B., Kaewkrajang, P., Shiono, T., Praserthdam, P., 2004b. Supporting effects of silica-supported methylaluminoxane (MAO) with zirconocene catalyst on ethylene/1-olefin copolymerization behaviors for linear low-density polyethylene (LLDPE) production. Industrial & Engineering Chemistry Research 43, 7959.

Jongsomjit, B., Kaewkrajang, P., Wanke, S.E., Praserthdam, P., 2004c. A comparative study of ethylene/1-olefin copolymerization with silane-modified silica-supported MAO using zirconocene catalysts. Catalysis Letters 94, 205.

Jongsomjit, B., Chaichana, E., Praserthdam, P., 2005a. LLDPE/nano-silica composites synthesized via in situ polymerization of ethylene/1-hexene with MAO/metallocene catalyst. Journal of Material Science 40, 2043.

Jongsomjit, B., Ngamposri, S., Praserthdam, P., 2005b. Catalytic activity during copolymerization of ethylene and 1-hexene via mixed TiO_2/SiO_2-supported MAO with rac-Et[Ind]$_2$ZrCl$_2$ metallocene catalyst. Molecules 10, 672.

Jongsomjit, B., Ngamposri, S., Praserthdam, P., 2005c. Role of titania in TiO_2-SiO_2 mixed oxides-supported metallocene catalyst during ethylene/1-octene copolymerization. Catalysis Letters 100, 139.

Jongsomjit, B., Ngamposri, S., Praserthdam, P., 2005d. Application of silica/titania mixed oxide supported zirconocene catalyst for synthesis of linear low-density polyethylene. Industrial & Engineering Chemistry Research 44, 9059.

Kogelbauer, A., Weber, J.C., Goodwin Jr., J.G., 1995. The formation of cobalt silicates on Co/SiO_2 under hydrothermal conditions. Catalysis Letters 34, 259.

Luyt, A.S., Molefi, J.A., Krump, H., 2006. Thermal, mechanical and electrical properties of copper powder filled low-density polyethylene composites. Polymer Degradation and Stability 91, 1629.

Nawang, R., Danjaji, I.D., Ishiaku, U.S., Ismail, H., Mohd Ishak, Z.A., 2001. Mechanical properties of sago starch-filled linear low-density polyethylene (LLDPE) composites. Polymer Testing 20, 167.

Randall, J.C., 1989. A review of high-resolution liquid ^{13}carbon nuclear magnetic resonance characterizations of ethylene-based polymer. Journal of Macromolecular Science Reviews in Macromolecular Chemistry and Physics C29, 201.

Verbeek, C.J.R., 2002a. Verbeek, C.J.R. Highly filled polyethylene/phlgopite composites. Materials Letters 52, 453.

Verbeek, C.J.R., 2002b. Effect of preparation variables on the mechanical properties of compression-molded phlogopite/LLDPE composites. Materials Letters 56, 226.

Available online at www.sciencedirect.com
ScienceDirect

Materials Chemistry and Physics 100 (2006) 445–450

MATERIALS CHEMISTRY AND PHYSICS

www.elsevier.com/locate/matchemphys

Preparation and phase transformation behavior of χ-alumina via solvothermal synthesis

Okorn Mekasuwandumrong [a,*], Varong Pavarajarn [b], Masashi Inoue [c], Piyasan Praserthdam [b,*]

[a] *Department of Chemical Engineering, Faculty of Engineering and Industrial Technology, Silpakorn University, Nakorn Pathom 73000, Thailand*

[b] *Research Center on Catalysis and Catalytic Reaction Engineering, Department of Chemical Engineering, Faculty of Engineering, Chulalongkorn University, Bangkok 10330, Thailand*

[c] *Department of Energy and Hydrocarbon Chemistry, Graduate School of Engineering, Kyoto University, Kyoto 606-8077, Japan*

Received 9 August 2005; received in revised form 21 November 2005; accepted 23 January 2006

Abstract

Solvothermal reaction of aluminum isopropoxide (AIP) in mineral oil at 250–300 °C over 2 h duration provides χ-alumina powder, which transforms directly to α-alumina after calcination at high temperature. The mechanism of the crystallization process appears to be the initial formation of a spherical complex which subsequently decomposes further to precipitate a solid. This mechanism is suggested by XRD, IR, TG/DTA, SEM and TEM characterization of the powder formed. χ-Alumina attains a critical crystallite size around 15 nm through accretion on calcination and then transforms directly to α-alumina through nucleation and growth process. Direct α-phase transformation of χ-alumina powders rather than passage through κ-alumina can be explained by the absence of the cation contamination and the higher crystallinity of χ-alumina in the AIP decomposition process.

© 2006 Elsevier B.V. All rights reserved.

Keywords: Solvothermal; Direct transformation; χ-Alumina

---

1. Introduction

Alumina is one of the most common crystalline materials used in many applications such as adsorbents, coatings, soft abrasives, catalyst and catalyst support [1–3] due to its fine particle size, high surface area and catalytic activity. The structural stability of alumina also makes it an important constituent of many protective oxides formed on the surface of high temperature metals and alloys.

There are many metastable polymorphs of transition alumina, including χ-alumina. χ-Alumina is normally prepared by the dehydration of gibbsite (<200 nm) [3–5]. It transforms to κ-alumina at temperature around 650–750 °C before final transformation to α-alumina at 1000–1100 °C. Both transformations lead to loss in the surface area and changes in surface properties. Three different unit cells have been proposed for χ-alumina. Stumpf et al. [6] suggested that χ-alumina has a cubic unit cell with lattice parameter of 7.95 Å, whereas other researchers [4] proposed hexagonal unit cells with either $a = 5.56$ Å and $c = 13.44$ Å or $a = 5.57$ Å and $c = 8.64$ Å. Hexagonal χ-alumina possess a layered structure, in which the hexagonal arrangement of oxygen is inherited from the structure of gibbsite and aluminum occupies octahedral sites within the hexagonal structure.

Recently, Inoue et al. [7–10] have examined the thermal decomposition of metal alkoxides in inert organic solvents, e.g. glycols, and demonstrated that various kinds of novel crystalline product, including χ-alumina, can be directly obtained without bothersome procedures such as purification of the reactants or handling in inert atmosphere.

Nanocrystalline χ-alumina prepared from the thermal decomposition of AIP in inert organic solvent has high thermal stability. It transforms directly to α-alumina at the temperature around 1150 °C, without passing into the κ-phase [7,11,12], resulting in neither the loss in surface area nor the change in surface properties. Moreover, the abrupt crystal growth

---

[*] Corresponding authors. Tel.: +66 63116537; fax: +66 34219368.
E-mail address: okornm@yahoo.com (O. Mekasuwandumrong).

0254-0584/$ – see front matter © 2006 Elsevier B.V. All rights reserved.
doi:10.1016/j.matchemphys.2006.01.040

Table 1
The physical properties of as-synthesized products obtained by the thermal decomposition of AIP in mineral oil in various reaction conditions

Reaction conditions		Phase	Crystallite size (nm)	S_{BET} ($m^2 g^{-1}$)	S_t ($m^2 g^{-1}$)[a]	Pore volume ($cm^3 g^{-1}$)[b]	Mode pore diameter (nm)[c]
Temperature (°C)	Time (h)						
250	0	Amorphous	–	7	7	0.03	11.8
250	2	χ-Alumina	9	192	186	0.64	13.3
250	6	χ-Alumina	10.8	149	189	0.43	11.5
270	2	χ-Alumina	10.2	180	210	0.52	11.5
300	2	χ-Alumina	9.4	124	138	0.45	14.2

[a] Calculated from the initial slope of the *t*-plot.
[b] Total nitrogen uptake at relative pressure of 0.98.
[c] Calculated from the desorption branch of the isotherm using the BJH method.

occurring during phase transformation can be effectively controlled. Therefore, nanocrystalline α-alumina can be simply obtained via the direct transformation from nanocrystalline χ-alumina. In this paper, we provide results for the reaction of AIP in mineral oil, including morphology of the synthesized particles and the phase transformation behavior.

2. Experiment

2.1. Sample preparation

Twenty-five grams of aluminum isopropoxide (AIP; Aldrich; >97%) was suspended in 100 ml of mineral oil (liquid paraffin; Ajax; specific gravity 0.830–0.890; CAS No. 8012-95-1) in a test tube, which was then set in a 300 ml autoclave. In the gap between the test tube and the autoclave wall, 30 ml of mineral oil was added. The autoclave was purged completely by nitrogen and heated up to the desired temperature, in the range of 250–300 °C, at a rate of 2.5 °C min^{-1}, and held at that temperature for the desired period of time (0–2 h). After the mixture was cooled down, the resulting powders were repeatedly washed with acetone and dried in air.

Parts of the product obtained was calcined in a box furnace by heating-up to the desired temperature (1000–1200 °C) at a rate of 10 °C min^{-1}. The calcination process was held at that temperature for 1 h.

2.2. Characterization

Powder X-ray diffraction (XRD) was measured on a SIEMENS XRD D5000 using Cu Kα radiation. The crystallite size was calculated from the Scherrer equation. The value of the shape factor, *K*, was taken to be 0.9 and α-alumina was used as an external standard. Infrared (IR) Spectra were recorded on a NICOLET FT-IR Impact 400 spectroscopy using an ex situ IR technique. The thermal behavior of the samples were analyzed on a Perkin-Elmer Diamond TG/DTA thermal analyzer at a heating rate of 10 °C min^{-1} in a 40 ml min^{-1} flow of dried air. Nitrogen adsorption isotherm and BET surface area of the samples were measured by a micromeritics medel ASAP 2000 using nitrogen as the adsorbate. The primary particles of alumina samples were observed by a JEOL TEM-200cx transmission electron microscope operated at 100 kV. Morphologies of alumina products were observed on JEOL scanning electron microscope.

3. Results and discussions

Table 1 summarizes the physical properties of obtained products before calcination. The products synthesized from the decomposition of AIP in mineral oil at 250, 270 and 300 °C with a holding time exceeding 2 h are χ-alumina, while the product obtained from heating the system up to 250 °C without holding time is amorphous. The amorphous product has much lower BET surface area and pore volume than all crystalline products. χ-Alumina obtained by the reaction at 250 °C for 2 h has the highest BET surface area and pore volume. When the reaction temperature is increased or the holding time is prolonged, BET surface area and pore volume of the obtained product is decreased by the coagulation of primary particles due to thermal effect.

The IR spectra of the products are shown in Fig. 1. All as-obtained powders show two adsorption bands attributed to water of crystallization at 3500–3200 cm^{-1} (υ(OH)) and 1640 cm^{-1} (δ(OH)) [13]. The amorphous powder obtained by quenching from 250 °C shows a strong adsorption bands at 1340–1470 cm^{-1} due to the isopropyl hydrocarbon groups [13]. As the holding time or reaction temperature is increased, the adsorption bands due to the organic group decrease and eventually disappear. The characteristic bands of boehmite were detected at 773 and 615 cm^{-1} [10] in the products obtained from 2 h reaction at 250 and 300 °C. This observation can be explained by the formation of boehmite by hydrolysis of AIP with water produced during the reaction.

Fig. 2 shows the results from the thermogravimetric analysis, i.e. TGA and DTA plots, of all powders prepared in mineral oil using various reaction conditions. Two weight decrease processes were detected from the amorphous powder corresponding on one endothermic and exothermic process. The first decrease in mass at around 80–200 °C, accompanied by the endothermic peak in DTA signal, is attributed to the desorption of physisorbed water. The second sharp mass decrease in TGA plot with sharp exothermic peak in DTA plot at around 300 °C is attributed to the combustion of organic moiety. The overall mass loss of this

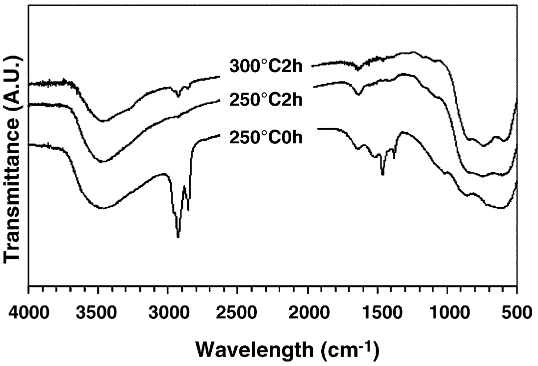

Fig. 1. IR spectra of as-synthesized products at various reaction conditions.

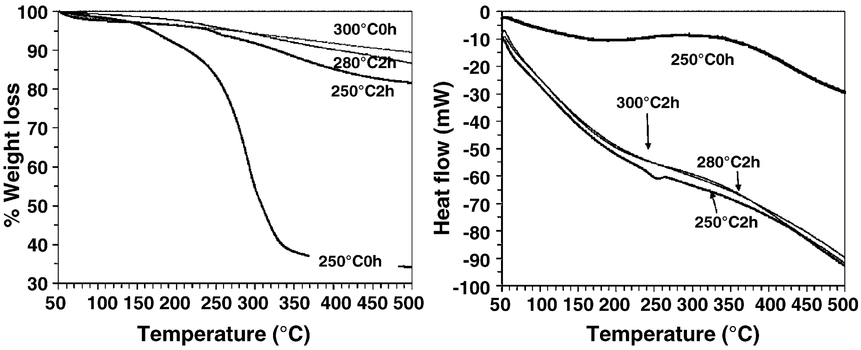

Fig. 2. TG and DTA data of the as-synthesized products.

amorphous sample is around 45%, which is lower than theoretically loss for AIP decomposition (75%). It is indicated that the starting AIP partially decomposes in mineral oil during the heating-up process. The remaining organic moieties from the partial decomposition of AIP reside in the amorphous product.

The nitrogen adsorption isotherms of as-synthesized products are shown in Fig. 3. All the crystalline samples exhibit the hysteresis loop with type-A adsorption characteristic, which is corresponding to the presence of two-ended tabular pore structure. On the other hand, the amorphous product shows the type-E hysteresis loop, which is an indication for the presence of tabular, through short pores with winded parts of various widths [14,15]. These pores are formed among the primary particles of alumina. Fig. 4 presents the pore size distribution of as-synthesized. All crystalline products exhibited the typical characteristic of mesopore system with pore size around 10 nm. It is shown that all products have narrow size distribution.

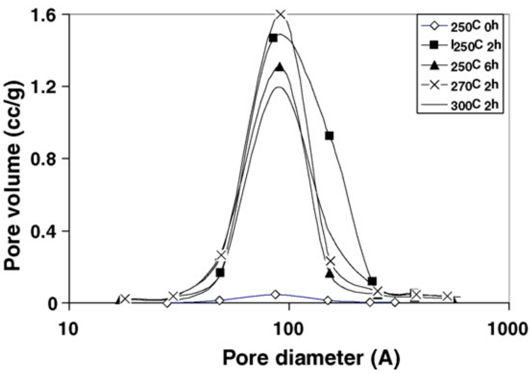

Fig. 4. Pore size distribution of as-synthesized product.

Fig. 5 shows the morphologies of as-synthesized and calcined samples observed by SEM. Spherical particles with average diameter around 1.8 μm were observed in the amorphous products prepared by quenching the reaction after the temperature had reached 250 °C (Fig. 5a). For the reaction with the holding time prolonged to 2 h, similar spherical particles in the products can still be observed. However, the average size of the particles decreases to 1.2 μm (Fig. 5b). These particles are secondary aggregates of nanocrystalline χ-alumina. With the increase of reaction temperature to 300 °C, size of the secondary particles further decreases to 1 μm (Fig. 5c). The results suggest that AIP decomposes stepwise in the inert solvent during heating-up

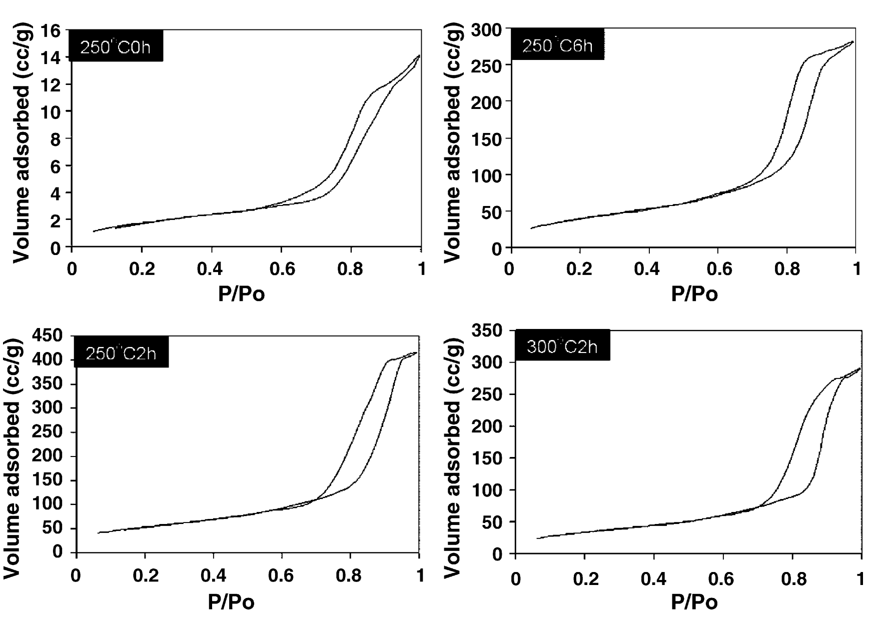

Fig. 3. The nitrogen adsorption isotherms of as-synthesized products.

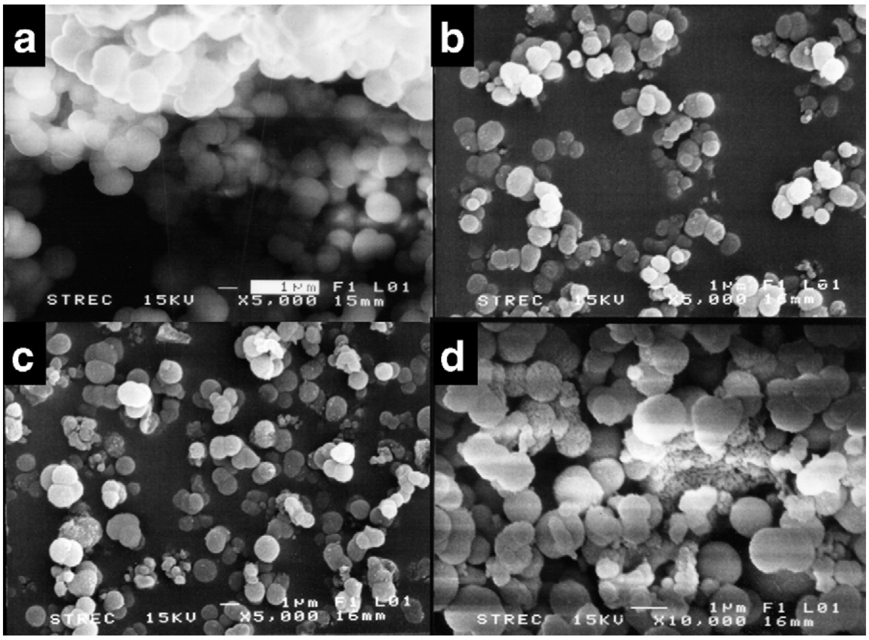

Fig. 5. SEM images: (a) as-synthesized product prepared by quenching reaction in mineral oil at 250 °C, (b) as-synthesized product prepared in mineral oil at 250 °C for 2 h, (c) as-synthesized product prepared in mineral oil at 300 °C for 2 h and (d) product (b) calcined at 1150 °C.

process, which results in an intermediate complex suspending in mineral oil. SEM micrographs confirms that this complex assumes a spherical shape. During the holding period, the complex further decomposes giving the nanocrystalline χ-alumina aggregated in form of spherical particles. The decrease in particle size with the increase in holding time and reaction temperature is due to the loss of the organic moiety in the complex by further decomposition. In this case, there are two nucleation processes. The first nucleation process is the formation of tiny droplets of the intermediate complex. This process is related to the salting out phenomena. During the partial decomposition of organic moieties, the decomposed intermediate is supersaturated in the solution and it is salted out forming the glassy droplets. Because the number of droplets formed in mineral oil is small, the droplets grow and large spherical particles are obtained. The second nucleation step is the formation tiny crystallites of χ-alumina. The morphology of products obtained in this work is different from χ-alumina obtained from the reaction in toluene [12]. This result will be further discussed.

According to Derjaguin–Landua–Verwey–Overbeek (DLVO) theory, the energy barrier between two particles, which inhibit agglomeration, is expressed as follow:

$$V_b = \left(\frac{A\kappa\alpha}{12}\right) + 2\pi\varepsilon_0\varepsilon_r\kappa\alpha\phi^2$$

where A is the effective Hamaker constant, κ the Debye–Huckel parameter, α the particle diameter, ε_0 the permittivity in the free space, ε_r the dielectric constant of the continuous phase and ϕ is the particle surface potential. Because of the constant ionic strength of the solvent, ε_0 and κ is constant, the maximum repulsive force estimated from the second term of the right hand side of the equation ($2\pi\varepsilon_0\varepsilon_r\kappa\alpha\phi^2$) is determined by the dielectric constant, particle size and repulsive force. Mineral oil (liquid paraffin) is the mixtures of long straight chain hydrocarbon produced as the bottom product from distillation. The dielectric constant of long chain hydrocarbon is around 1.9–2 ($C_{13}H_{28} = 2.02$, $C_{14}H_{30} = 2.05$, $C_{19}H_{40} = 2.09$), which lower than toluene (2.379). According to the quite low dielectric constant of mineral oil, the particles become discrete and form spherical particles. Fang and Chen [16] reported that, for the synthesis of TiO_2 by the reaction of $TiCl_4$ in a mixed solvent of *n*-propanol and water, the spherical particles were

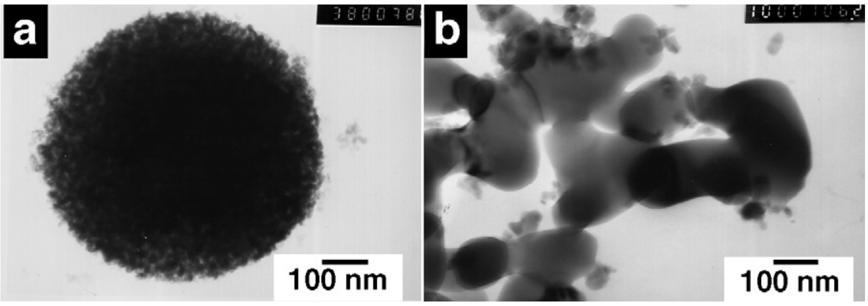

Fig. 6. TEM images: (a) as-synthesized product prepared in mineral oil at 250 °C for 2 h and (b) product (a) calcined at 1150 °C.

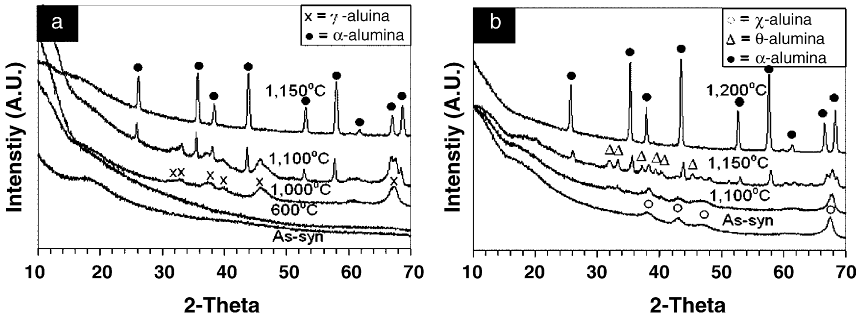

Fig. 7. The XRD patterns of powder synthesized by the reaction of AIP in mineral oil calcined at various reaction conditions: (a) 250 °C for 0 h and (b) 300 °C for 2 h.

formed in the solvent with *n*-propanol/water ratio resulting in the lowest value of dielectric constant.

Transmission electron micrographs of the as-obtained powder and calcined powder are shown in Fig. 6. The as-synthesized χ-alumina products are comprised of agglomerated primary particles having average diameter around 10 nm. As shown in Table 1, the crystallite size calculated by XRD peak broadening, using the Scherrer equation, is 9 nm. Good agreement between both values indicates that each primary particle observed by TEM is a single crystal of χ-alumina.

The XRD patterns of calcined product are shown in Fig. 7. The amorphous product remains amorphous even after calcination at 600 °C (Fig. 7a). However, after calcination at 1000 °C, γ-alumina is observed. The α-phase transformation takes place at temperature around 1150 °C and completes at 1200 °C. It should be noted that the peak at 42.5°, which is corresponding to χ-alumina, is not detected. This indicates that χ-alumina is not formed by calcination of the amorphous product. Therefore, the formation of χ-alumina occurs only in the inert organic solvent. For the calcination of χ-alumina obtained from thermal decomposition of AIP at 300 °C for 2 h (Fig. 7b), χ-alumina transforms to α-alumina directly at temperature around 1100 °C. No κ-alumina was detected. The χ-to-α phase transformation is completed at temperature around 1200 °C. Phase transformation sequences of products obtained from other reaction conditions are summarized in Table 2.

After calcination, the secondary particles still remain spherical with unchanged average particle size, regardless of the crystalline phase (see Fig. 5d). Some finger-like primary particles aggregating on the spherical secondary particles were also observed after the calcination at 1200 °C. TEM micrographs of calcined samples clearly show two groups of primary particles after the phase transformation. The first group is the spherical χ-alumina particles, which do not transform to α-alumina. These particles have crystallite size calculated from the Scherrer equation that is the same as particle size observed by using TEM. The second group of primary particles is the finger-like α-alumina transformed from the low-temperature transition alumina nanocrystals via the nucleation and growth mechanism (see Fig. 6b).

The direct phase transformation of χ- to α-alumina is a specific property for powders prepared by the decomposition of AIP in an inert organic solvent. In our previous work, it has been proposed that the direct phase transformation is the result from the absence of contaminating cations in crystals, as well as high crystallinity of the synthesized product due to the small amount of water adsorbed on the surface. Chou and Nieh [17] have reported that the nucleation of α-alumina occurs along (2 2 0) crystallographic plane of γ-alumina in nanocrystalline oxide synthesized by radio frequency reactive sputtering deposition. Johnston et al. [18] have reported that γ-alumina prepared by laser ablation synthesis directly transforms into α-phase and they have attributed that the particle size of the product is well below the grain size limit for super plastic alumina (500 nm). Bahlawane and Watanabe [19] prepared anhydrous alumina which transformed directly to α-alumina by sol–gel method. Shek et al. [20] have reported that amorphous powders prepared by oxidation of pure aluminum metal crystallize to γ-alumina, which directly transforms to α-alumina at 1370 K. They have attributed this result to the facilitation of nucleation of α-alumina by the strain relaxation of the transition alumina lattice. However, relaxation of the γ-alumina structure should decrease the energy level of γ-alumina and disturb the nucleation of more stable phases. Simpson et al. [21] have reported that samples prepared via electron-beam evaporation of alumina onto a sapphire substrate held at room temperature crystallize to γ-alumina, which transforms into α-alumina without formation

Table 2
The crystallite size calculated by the Scherrer equation and phase of the as-synthesized and calcined products

Reaction condition		Crystallite size and phase of alumina after treat at various temperatures (°C)				
Temperature (°C)	Time (h)	As-synthesized	1000	1100	1150	1200
250	0	– (Amorphous)	6.2 (γ)	16.5 (γ), 31.1 (α)	33.7 (α)	– (α)
250	2	9 (χ)	9.2 (χ)	9.6 (χ)	12.3 (χ), 36.4 (α)	68 (α)
250	6	10.8 (χ)	11.2 (χ)	12.5 (χ)	15.2 (χ), 39.2 (α)	77.2 (α)
270	2	10.2 (χ)	9.4 (χ)	10.3 (χ)	15.6 (χ), 33.5 (α)	97.5 (α)
300	2	9.4 (χ)	10.8 (χ)	14.2 (χ), 39.5 (α)	14.6 (χ), 41.3 (α)	44.7 (α)

of other intermediate phases. They have attributed this result to the epitaxial growth of α-alumina on the sapphire substrate. Ogihara et al. [22] have prepared monodispersed, spherical alumina by the controlled hydrolysis of aluminum alkoxide in a dilute solution containing octanol and acetonitrile. They have found that the amorphous product crystallizes to γ-alumina at 1000 °C which converted to α-alumina at 1150 °C without intermediate phase. However, they did not give any explanation for this result. It has also reported that γ-alumina formed by thermal decomposition of aluminum sulfate transforms into α-alumina directly [23–25].

The crystallite sizes of calcined products are summarized in Table 2. The crystallite size of is initially about 9–10 nm. χ-Alumina grows to 16 nm upon calcination but the growth stop at this size even after the calcination at high temperature. At higher calcination temperature, only α-alumina was observed. It is suggested that χ-alumina grows to the critical size and then abruptly transforms into α-alumina. The result suggests that the critical size of χ-alumina, beyond which it is unstable and undergoes phase transformation into α-alumina, is around 16 nm. Once the phase transformation takes place, the primary particles grow drastically and then become sluggish. The α-phase transformation is considered to occur through a nucleation and growth mechanism [26,27]. Investigations on the phase transformation after the crystallite size has reach the critical size have been reported by many researchers [28–30]. Yen et al. [28,29] have found that, during the phase transformation, there is a critical size for θ-alumina (around 22 nm) at the nucleation stage, which initiates the formation of α-alumina nucleus.

4. Conclusion

Thermal decomposition of AIP in mineral oil at temperature between 250 and 300 °C with holding time of 2 h results in the micro-spherical particles formed by agglomeration of nanocrystalline χ-alumina. On the contrary, the powder obtained during the heating-up process to 250 °C is amorphous. The fact that χ-alumina is not formed by the calcination of the amorphous intermediate confirms that χ-alumina is formed only by AIP decomposition in the inert organic solvent. It is suggested that a spherical particle of complex moieties forms through stepwise decomposition of AIP in the solvent. With the prolonged holding time or increased reaction temperature, this complex sheds organic moieties and solid-state phase of χ-alumina is formed. After calcination at high temperature, χ-alumina transformed to α-alumina directly. The crystallite size of χ-alumina is initially around 9–10 nm and grows upon the calcination to the critical size of 16 nm, beyond which χ-alumina transforms to α-alumina. This direct transformation behavior of nanocrystalline χ-alumina is attributed to the absence of cations and the less defect structure.

Acknowledgement

The author would like to thank the Thailand Research Fund (TRF) for their financial support.

References

[1] W.H. Gitzen, Alumina as a Ceramics Material, American Ceramic Society, Columbus, OH, 1970.
[2] G.M. Pajonk, Appl. Catal. A: Gen. 72 (2) (1991) 217–266.
[3] K. Wefers, G.M. Bell, Oxides and Hydroxides of Alumina, Alcoa, Bauxite, AR, 1972.
[4] H. Saalfeld, Structure Phases of Dehydrated Gibbsite, Elsevier, The Netherlands, 1961.
[5] G.W. Brindley, J.O.T. Choe, Am. Miner. 46 (7–8) (1961) 771785.
[6] H.C. Stumpf, A.S. Russell, J.W. Newsome, C.M. Tucker, Ind. Eng. Chem. 42 (7) (1950) 1398–1403.
[7] M. Inoue, H. Kominami, T. Inui, J. Am. Ceram. Soc. 75 (9) (1992) 2597–2598.
[8] M. Inoue, H. Kominami, T. Inui, Appl. Catal. A: Gen. 121 (1) (1995) L1–L5.
[9] S. Iwamoto, K. Saito, M. Inoue, K. Kagawa, Nano Lett. 1 (8) (2001) 417–421.
[10] P. Pratherthdam, M. Inoue, O. Medkasuvandumrong, W. Thanakulrangsan, S. Phatanasri, Inorg. Chem. Commun. 3 (11) (2000) 671–676.
[11] O. Mekasuwandumrong, P.L. Silveston, P. Praserthdam, M. Inoue, V. Pavarajarn, W. Tanakulrungsank, Inorg. Chem. Commun. 6 (7) (2003) 930–934.
[12] O. Mekasuwandumrong, H. Kominami, M. Inoue, P. Praserthdam, J. Am. Ceram. Soc. 87 (8) (2004) 1543–1549.
[13] D.A. Skoog, J.J. Leary, Principles of Instrumental Analysis, Saundres College Publishing, Philadelphia, San Diego, 1992.
[14] B.C. Lippens, J.H. de Boer, J. Catal. 4 (3) (1965) 319–323.
[15] B.C. Lippens, J.H. de Boer, J. Catal. 3 (1) (1964) 32–37.
[16] C. Fang, Y. Chen, Mater. Chem. Phys. 78 (3) (2003) 739–745.
[17] T.C. Chou, T.G. Nieh, J. Am. Ceram. Soc. 74 (9) (1991) 2270–2279.
[18] G.P. Johnston, R. Muenchausen, D.M. Smith, W. Fahrenholtz, S. Foltyn, J. Am. Ceram. Soc. 75 (12) (1992) 3293–3298.
[19] N. Bahlawane, T. Watanabe, J. Am. Ceram. Soc. 83 (9) (2000) 2324–2326.
[20] C.H. Shek, J.K.L. Lai, T.S. Gu, G.M. Lin, Nanostruct. Mater. 8 (5) (1997) 605–610.
[21] T.W. Simpson, Q. Wen, N. Yu, D.R. Clarke, J. Am. Ceram. Soc. 81 (1) (1998) 61–66.
[22] T. Ogihara, H. Nakagawa, T. Yanagawa, N. Ogata, K. Yoshida, J. Am. Ceram. Soc. 74 (9) (1991) 2263–2269.
[23] D.W. Johnson, F.J. Schnettler, J. Am. Ceram. Soc. 53 (8) (1970) 440–444.
[24] E. Kato, K. Daimon, M. Nanbu, J. Am. Ceram. Soc. 64 (8) (1981) 436–445.
[25] M.D. Sacks, T.-Y. Tseng, S.Y. Lee, Ceram. Bull. 63 (2) (1984) 301–310.
[26] D.S. Tucker, J. Am. Ceram. Soc. 68 (7) (1985) C163–C164.
[27] F.W. Dynys, J.W. Halloran, J. Am. Ceram. Soc. 65 (9) (1982) 442–448.
[28] F.S. Yen, H.L. Wen, Y.T. Hsu, J. Crystal Growth 233 (4) (2001) 761–773.
[29] F.S. Yen, H.S. Lo, H.L. Wen, R.J. Yang, in press.
[30] R.B. Bagwell, G.L. Messing, P.R. Howell, J. Mater. Sci. 36 (7) (2001) 1833–1841.

Available online at www.sciencedirect.com
ScienceDirect
ELSEVIER
Ceramics International xxx (2006) xxx–xxx
CERAMICS INTERNATIONAL
www.elsevier.com/locate/ceramint

Preparation of ZnO nanorod by solvothermal reaction of zinc acetate in various alcohols

Parawee Tonto[a], Okorn Mekasuwandumrong[b,*], Suphot Phatanasri[a,*], Varong Pavarajarn[a], Piyasan Praserthdam[a]

[a] *Center of Excellence on Catalysis and Catalytic Reaction Engineering, Department of Chemical Engineering, Faculty of Engineering, Chulalongkorn University, Bangkok 10330, Thailand*
[b] *Department of Chemical Engineering, Faculty of Engineering and Industrial Technology, Silpakorn University, Nakorn Pathom 73000, Thailand*

Received 26 April 2006; received in revised form 10 May 2006; accepted 22 August 2006

Abstract

Solvothermal reaction of zinc acetate in various alcohols resulted in the formation of zinc oxide (ZnO) nanorods. The effects of reaction conditions on the product morphology as well as crystallization mechanism were investigated by using X-ray diffraction (XRD), infrared spectroscopy (IR), scanning electron microscopy (SEM), energy dispersive X-ray spectroscopy (EDS) and transmission electron microscopy (TEM) techniques. It was found that average diameter and length of the nanorods increased with an increase in reaction temperature or the initial concentration of zinc acetate. On the contrary, the aspect ratio of the product depended upon type of alcohol used as the reaction medium. The aspect ratio of ZnO nanorods increased from 1.7 to 5.6 when the alcohol was changed from 1-butanol to 1-decanol. An investigation of the reaction mechanism suggested that the formation of ZnO nanorods was initiated from the esterification reaction between zinc acetate precursor and alcohol to form ZnO seeds.

© 2006 Elsevier Ltd and Techna Group S.r.l. All rights reserved.

Keywords: D. ZnO; Nanorod; Alcohol; Solvothermal

1. Introduction

Nanostructured materials have received increasing attention due to their potential uses as active components or interconnects in nanoscaled electronic, optical, optoelectronic, electrochemical, and electromechanical devices [1]. One material that has been in great interest from wide range of technological field associated with nanotechnology is zinc oxide (ZnO) [2]. ZnO is a material with large direct band gap (3.3 eV) and excellent chemical and thermal stability. It has unique optical and acoustic properties, as well as electronic properties of the II–VI semiconductor with large exciton binding energy (60 meV) [3]. Therefore, zinc oxide has been used in various applications, e.g. as varistor, gas-sensor, catalyst and pigment. According to great function of zinc oxide, several techniques have been proposed for zinc oxide synthesis, e.g. hydrothermal synthesis [4,5], thermal decomposition method [6,7], sol–gel synthesis [8], flame spray pyrolysis [9], and precipitation method [10].

Control of the particle shape is another concern for nanostructured material synthesis because electrical and optical properties of nanomaterials depend sensitively on both size and shape of the particles. Therefore, it is desired to synthesize nanomaterial in a controllable shape and size by simple approach. For zinc oxide particles, various shapes including nanorods [11–13], whiskers [14,15] and nanowires [16] have been successfully prepared. However, it was the result from different synthesis methods under different preparation conditions [17].

In this study, the solvothermal method was employed to synthesize ZnO nanorods. This technique is based on thermal decomposition of organometallic compound in organic solvent and has been successfully applied for the synthesis of various types of nanosized metal oxide with large surface area, high crystallinity and high thermal stability [18–20]. The influences of reaction conditions, i.e. type of solvent, concentration and

---

[*] Corresponding authors. Tel.: +66 63116537; fax: +66 34219368.
E-mail addresses: okornm@yahoo.com (O. Mekasuwandumrong), Suphot@thaipeginner.com (S. Phatanasri).

0272-8842/$30.00 © 2006 Elsevier Ltd and Techna Group S.r.l. All rights reserved.
doi:10.1016/j.ceramint.2006.08.003

Please cite this article in press as: P. Tonto et al., Preparation of ZnO nanorod by solvothermal reaction of zinc acetate in various alcohols, Ceram. Int. (2006), doi:10.1016/j.ceramint.2006.08.003